Supersonic Braking Devices for Upper Stage Recovery - Design and aerodynamic assessment of RocketHandbrake

Christian Hantz[a], Junnai Zhai[a], Fynn Barz[b], Atra Gemilang[c], Josef Klevanski[a], Ansgar Marwege[a], Ali Gülhan[a]

[a]*DLR / Institute of Aerodynamics and Flow Technology / Supersonic and Hypersonic Technologies Department, Linder Hoehe, Köln, 51147, Germany*

[b]*DLR / Institute of Aerodynamics and Flow Technology / Spacecraft Department, Lilienthalplatz 7, Braunschweig, 38108, Germany*

[c] *POLARIS Raumflugzeuge GmbH, Zum Panrepel 11, 28307 Bremen, Germany*

Abstract

Reusability in spaceflight represents a major challenge from a technical perspective, with an economical cost savings promise. Multiple European projects (e.g. RETALT, RETPRO, Themis, SALTO and CALLISTO) investigated and keep investigating reusability of first stages. While retro propulsion became a standard approach for first stage deceleration, for upper stages it comes with large fuel consumptions due to their high orbital velocities and energy level. Complementing these research efforts, the project "RocketHandbrake" investigates upper stage reusability, using Supersonic Braking Devices (SBD) for aerodynamic braking with the objective to reach full reusability of future European launch vehicles. SBD´s enable high angle of attack reentries, resulting in significant drag forces that are used for an atmospheric deceleration. However, this concept comes with the mass penalty for the SBD as well as the required thermal protection system (TPS).
The ESA funded study "Supersonic Braking Devices for Upper Stage Recovery – RocketHandbrake", led by DLR together with Polaris and Deimos, aims to understand the key technologies required for a reusable upper stage configuration under a multitude of aspects, and to improve prediction tools for the concept. Based on a reference launcher configuration defined at the beginning of the project, the SBD are defined, analyzed and tested. Hereby a close collaboration between the different design areas of aerodynamics, thermal, structures, mechanisms and GNC is required to enable a feasible mission profile and a coherent design to be able to handle

unsteady effects and thermal issues.
This paper presents the work performed by DLR in RocketHandbrake during the detailed design and analysis phase up to the final wind tunnel testing at DLR´s Trisonic Wind Tunnel Cologne (TMK) in the context of aerodynamic analysis. Initially, the Supersonic Braking Devices are rescaled on the first phase´s outcomes, providing the new outer mold line for the numerical analysis. An Aerodynamic Database (AEDB), as well as a smaller Aerothermal Database (ATDB) is generated. The wind tunnel model is designed, manufactured and subsequently tested. As a final step, the aerodynamic analyses are combined and evaluated.

Keywords: Supersonic Braking Devices, reusable launch vehicle, aerodynamic braking, upper stage

1 Introduction

The ESA TRP project ‘RocketHandbrake’ started in 2021 and investigates the reusability of upper stages and boosters reentering earth´s atmosphere. More specifically, high angle of attack aerodynamic deceleration under the aid of supersonic braking devices (SBD) is studied. This eliminates the need for additional Supersonic Retro Propulsion (SRP) fuel – besides the final landing burn, however, at the cost of SBD.
The project was described first in 2022 [1], giving an overview of the project and outcomes of the first project phase. Three companies are part of the project RocketHandbrake, namely the German Aerospace Center (DLR) in Cologne and Braunschweig (Germany), Polaris in Bremen (Germany) and Deimos Space in Madrid (Spain).
The main objective of the project is to understand the key technologies required for a reusable upper stage configuration under a multitude of aspects, and to improve prediction tools. The project also features wind tunnel tests to generate data for physical understanding and validation of numerical tools.
The concept chosen for evaluation utilizes the fuselage as a main drag generator, together with small flaps in the front and rear to provide the required control authority. The vehicle re-enters earth’s atmosphere at high angles of attack, thus requiring a suitable Thermal Protection System (TPS) for the fuselage and flaps, as well as corresponding Guidance Navigation and Control (GNC) routines. This concept is based on the approach taken by SpaceX with their Starship launcher.

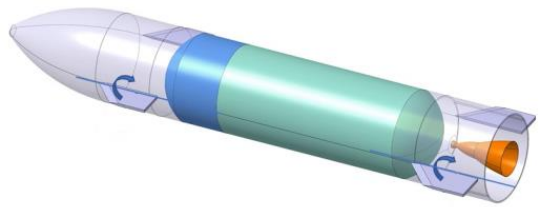

Figure 1: General Concept Layout

It shall be emphasized, that the project does not aim to develop the launcher under study completely, but to clarify and focus on the required aerodynamic control surfaces, the entailed aerodynamics and resulting flow physics, flight dynamics, control laws, and structures.

The project RocketHandbrake is divided into four phases:

The first phase consisted of the initial design and assessment of two configurations, yielding preliminary launcher specifications tailored to the concept under study, based on the publicly available and published literature. At the end of the first phase, a so-called Ariane Next -like (ANL) configuration was chosen for further evaluation. (The term '-like' is used to indicating the usage of own assumptions, calculations and definitions, likely deviating from the real future Ariane Next launcher)

The second phase dealt with the detailed design and evaluation of the Ariane Next reusable upper stage in terms of:
• Aerodynamics
• Aerothermodynamics and Heat Loads
• Structures
• Flight dynamics and Control laws

Phase three covered the preparation of the wind tunnel test, namely the design of the model, its manufacturing and the test preparation.

The last phase consists of the wind tunnel test execution and its evaluation. The tests were carried out in the Trisonic Wind Tunnel Cologne (TMK) at DLR´s Supersonic and Hypersonic Technologies Department. Furthermore, the overall project results are summarized and evaluated to determine the developed system performance. Additionally, a roadmap for technology maturation is developed, pathing the way for further investigations but also

integration of the concept analyzed.

This paper focuses on the aerodynamic assessment of the Ariane Next configuration performed within the frame of the RocketHandbrake project, while also giving a short summary of the projects detailed design outcomes.

For further information please see the paper by Gabriele De Zaiacomo, Ascension Conference in Dresden, 2023, ASC-ABS-0024 “Mission Engineering and Control Design for the Recovery of a Heavy Launcher Upper Stage”. [2]

2 Detailed Design Summary of the upper stage with Supersonic Braking Devices

2.1 Supersonic Braking Devices

Supersonic Braking Devices (SBD), as described previously in [1], describe the control surfaces of the flight vehicle used to perform an aerodynamic braking maneuver within the atmosphere, by means of a high angle of attack descent. Thus, their main purpose is the moment generation required to reach and keep those high angles of attack required. Their mode of operation is to rotate in the length axis (x-axis, or close to it), but not to rotate like canards or ailerons in the axis of their span (y-axis), see also Figure 1.
Frontal and rear SBD do not need to have the same angle setting, but can be different to adjust the moments required. Additionally, a change of deflection between the left and right side could provide further steering or roll control

In short, the main purpose of the SBDs is not the drag generation, but the moment control of the fuselage.

2.2 Reference Concept Design

With sufficient moment control, the upper stage can be hold at high angles of attack during the aerodynamic descent. Thus, the cross-sectional area in the oncoming flow is maximized, as the fuselage is nearly perpendicular to the oncoming airflow, creating a large and meaningful drag force. Following this, the upper stage can brake aerodynamically while descending through the atmosphere, without the requirement for supersonic retro propulsion. For the landing, the vehicle needs to be rotated with the aid of the SBD and the main engine, which is then also used for the final deceleration at touch down.

The upper stage, including its Supersonic Braking Devices (SBD), also simply called flaps, is shown in Figure 2. They can be deflected (nearly) parallel to the length axis (x-axis) of the vehicle (see also Figure 1).

The Ariane Next launcher was used as a baseline for the application of the aerodynamic braking concept with supersonic braking devices, forming the Ariane Next -like concept analyzed in the project. The launcher specifications were taken from available, non-classified literature. Thus, important information like detailed engine specifications were not available and were estimated with the help of available tools and programs.

The main specifications of the Ariane Next configuration are (after Initial Design Phase 1, before Detailed Design Phase 2):

Ariane Next -like	***Data***	***Unit***
Nose to Base	57.5	m
Nosecone	7	m
1st stage	36.5	m
2nd stage	21	m
Engine Nozzle	< 2	m
Diameter (ø)	5.4	m
Design COG position (@ reentry)	10.9	m
Structure Mass	15’082	kg
Propellant Mass	123’440	kg
Takeoff mass	142’756	kg

Table 1 AN Launcher Dimensions

Further details are given in [1].

The detailed design yielded the general upper stage layout depicted in Figure 2, featuring four flaps, rotating along (or close to) the x-axis of the body. Their deflection angles, or dihedral angle, can be changed in the range from 0° to 90° independently, whereas 0° corresponds to the flaps pointing in opposite directions (—o—) and 90° to both pointing upwards (┗o┛). The main parameters of the reference shape are:

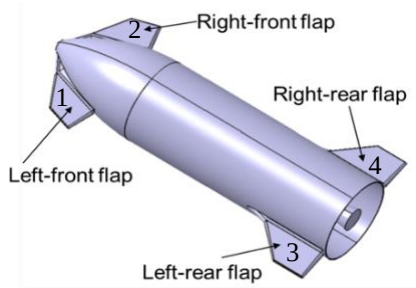

Figure 2 Ariane Next (AN) design

Table 2 Reference parameter definition

Parameter	**Formula**	**Value [Unit]**
Reference Length	$L_{ref} = D_{ref}$	5.4 [m]
Reference Area	$S_{ref} = \pi * D_{ref}^2 /4$	22.9022 [m²]

Table 3 Key upper stage parameters of Ariane Next

Length [m]	**Diameter [m]**	**Area front flap [m²]**	**Area rear flap [m²]**
20.731	5.4	4.023	5.370

Table 4 Flap number definition

Flap position	**Flap number**
Front Left	1
Front Right	2
Rear Left	3
Rear Right	4

2.3 Structures and Mechanisms

The structure of the flaps was designed, optimized and numerically analyzed based on the expected loads obtained via the aerodynamics and trajectory definitions. the flap structure design and actuator sizing only mechanical load cases are considered without thermal loads, since the flap structure is isolated by TPS. The actuator configurations were studied for optimum actuator load. The mass of the flaps is shown in Table 5. Furthermore, the actuation mechanism was defined and an actuator identified.

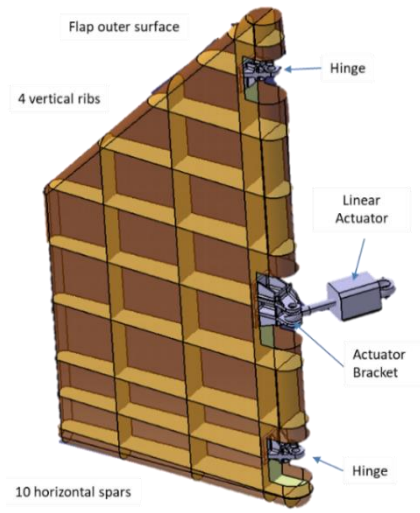

Figure 3 flap structure concept

Table 5 SBD mass contributions

No attachments, no TPS	Mass	Unit
Front Flap (each)	~ 110	kg
Rear Flap (each)	~ 170	kg
SBD (excl. actuation)	~ 560	kg

Preliminary sizing and analysis were also done for the fuselage and tank structure (see Figure 4). The analysis was focused on the most critical load cases for the preliminary sizing of the primary rocket structure with the consideration of structural dynamic effect in the analysis and simplification of the model. The factors for the structure analysis were defined and applied in the structure simulation model. The total dry mass of the vehicle is currently about 15 tons, including a mass increase due to refinement of 10%, a final dry mass of ~17 000 kg is expected. It shall be noted, that this mass estimation is based on a first loop analysis

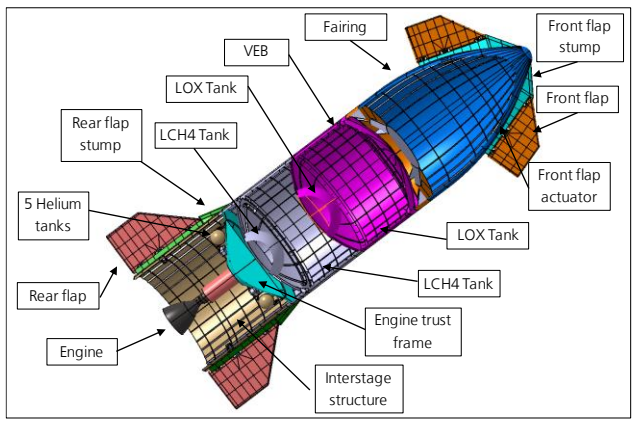

Figure 4 internal structure preview

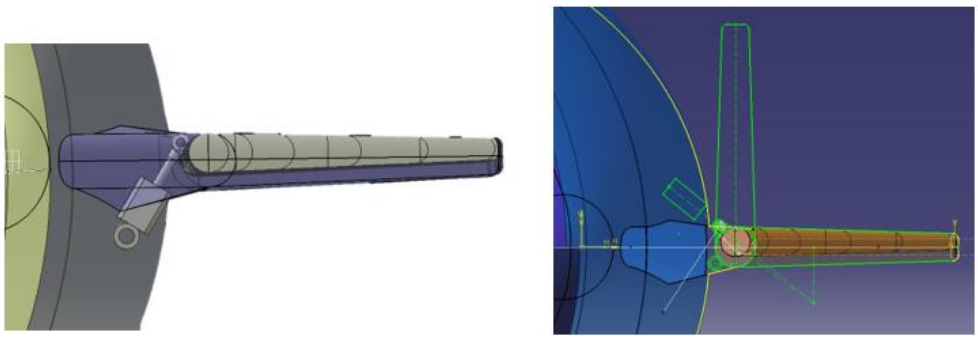

Figure 5 Two configurations of the kinematic system installation: actuator in in opposite direction of the re-entry face (left) and actuator towards the re-entry face (right)

Two configurations of actuator integration within the spacecraft were studied. The first configuration was studied with actuators placed in opposite direction of the re-entry face (leeward side) of the space craft on both front and rear flaps and a second configuration was studied with actuators placed towards the re-entry face (windward side) of the space craft (see Figure 5). In the second, leeward configuration the rear flaps were observed to undergo significantly higher loads and front flap were observed to undergo significantly lower loads at reference trajectory and thermal sizing trajectory respectively in comparison to first configuration. Thus, using a combination of both configurations with the windward actuator for the rear flap and leeward actuator for the front flap yields the best design for an optimal actuator sizing. Thus, configurations with the windward actuator for the rear flap and leeward actuator for the front flap yields the best design for an optimal actuator sizing.

Another outcome is the design, sizing, mass determination and comparison of the TPS variations to protect the upper stage against the high thermal loads and fluxes during aerodynamic braking and descent (see Figure 6). According to this study, the Leading Edges, Nose and Front Flap windward side require high temperature CMC protection. The combination of AFRSI at low temperature, metallic TPS at medium temperature and CMC at high temperature is applied for the SBD. As a result, the TPS configuration with AFRSI, Inconel HC and CMC were being selected as baseline. Considering manufacturability, it was found that the TPS mass increases by up to 20% (See Figure 7). The TPS mass was found to be around 4200 kg.

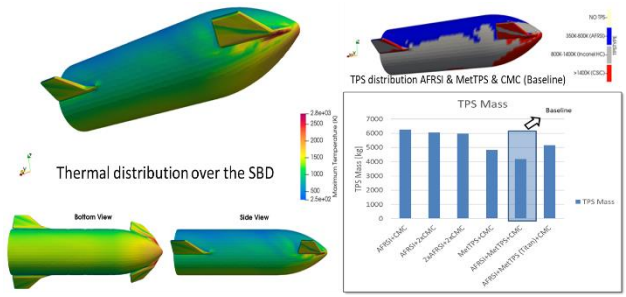

Figure 6 Thermal and TPS distribution over SBD

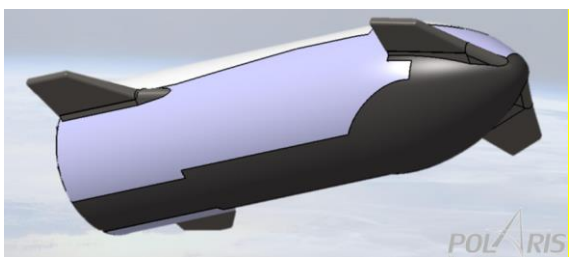

Figure 7 Manufacturable TPS Design

Outcomes:
The structure of the SBD was designed in detail with some simplification, yielding a sound design able to withstand the expected forces and moments, as well as the definition of the actuation system. The optimal actuation configuration for the flap kinematic system was identified. Furthermore, a TPS concept was designed for the worst-case scenario, the thermal sizing trajectory. Additionally, future design optimizations for the SBD and TPS were identified.

2.4 Mission Analysis, GNC & Flight Dynamics

The aerodynamic results were evaluated from a controls perspective, generating a reference trajectory which was later on updated using the AEDB 3.0. A thermal sizing trajectory was defined as the worst-case trajectory in terms of heat loads, providing the input for the TPS sizing. Mission Analyses were performed, creating possible entry corridor maps. It was found, that a feasible entry corridor exists, as long as the CoG stays within a defined range. The formulated control algorithms relate the classical control inputs like pitch, roll and yaw to the individual flap deflections forming the SBD, allowing an assessment of the vehicle control performance. The analysis

incorporated evaluating the control limits of the individual flaps, static and dynamic stability assessment and definition of the requirements for a stable and trimmable vehicle and entry corridor. Furthermore, entry conditions at earth´s interface point were defined and the longitudinal and lateral ranges capability assessed and verified. Further it was found that a Reaction Control System (RCS) is required, and it was therefore sized. The performance of the control solution was assessed carrying out multiple Monte Carlo flight dynamics simulations to verify the robustness of the proposed solutions.

For further information please see the paper by Gabriele De Zaiacomo, Ascension Conference in Dresden, 2023, ASC-ABS-0024 “Mission Engineering and Control Design for the Recovery of a Heavy Launcher Upper Stage”. [2]

3 Aerodynamics Data and Aerothermodynamic Data

Aerodynamic Databases store the aerodynamic coefficients of a flight vehicle and its configurations with variable control parameters (e.g. flap positions) for multiple flight conditions.

3.1 Aerodynamic Database (AEDB)

The latest AEDB 3.0 covers the sub-, trans- and supersonics of ten different configurations. Each configuration provides aerodynamic coefficients for 22 Angles of attack (0° to 90° in 5° steps and 120°, 150°, 180°), 7 Mach numbers (0.5, 0.7, 0.9, 1.2, 1.5, 3, 6) and two roll angles (0° and 10°). Thus, the database was built up by 3080 CFD calculation points.

The tested configurations are shown in Table 6.

Table 6 AEDB Configurations

Front Left	Front Right	Rear Left	Rear Right
0	0	0	0
0	0	60	60
0	0	90	90
30	30	30	30
30	30	60	60
60	60	0	0
60	60	30	30
70	70	20	20
90	90	0	0
Left – Right Asymmetric			
70	70	10	30

3.2 Calculation scheme, mesh and convergence

The numerical CFD simulations were performed with the hybrid structured-unstructured DLR Navier–Stokes solver TAU [3]. The TAU code is a second-order finite-volume flow solver for the Euler and Navier-Stokes equations. This work utilized the Spalart–Allmaras one equation eddy viscosity model [4] in the latest AEDB 3.0.

The mesh was found to be sufficient and the y+ value of the model is around

one. The convergence in terms of CD and CL is within the intended accuracy.

3.3 Uncertainty

The uncertainties were not evaluated numerically. Based on experience an uncertainty factor of 20% is defined. For coefficients going through zero, the minimum value would be identical, namely zero, thus the uncertainty shall be taken as uncertainty in the AoA. The uncertainty in AoA shall correspond to the uncertainty of the coefficient ± 5° away from the zero point

3.4 Results and its usage

The aerodynamic results are used for Mission Analysis, the Guidance Navigation and Control algorithms, as well as the Flight Dynamics simulations (For more details, see [2]).

A valuable information drawn from the AEDB is the effect of the COG on the CMy coefficient, shown in Figure 8 and Figure 9. It allows a quick assessment of the trimmability, stability and controllability of the vehicle.

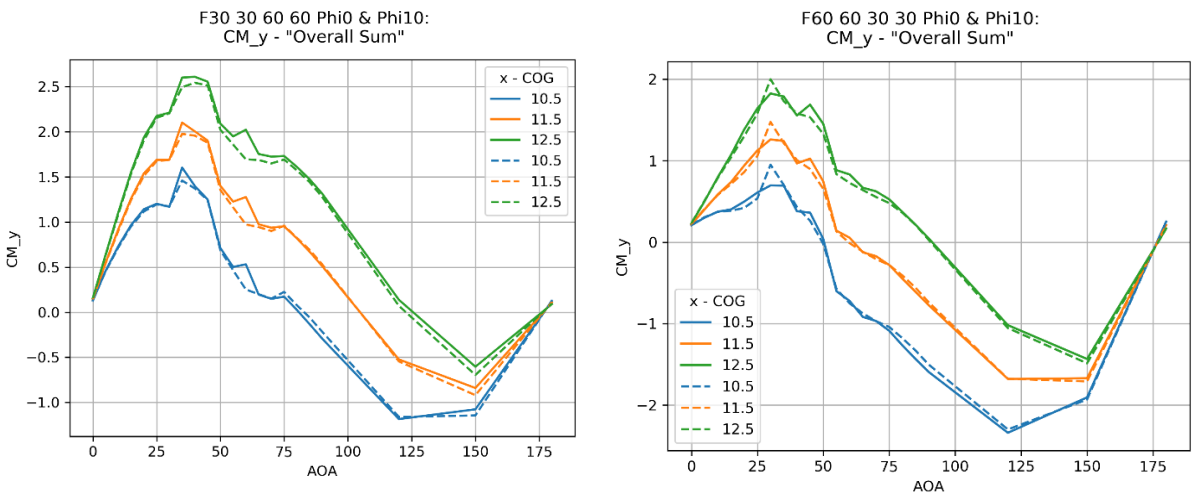

Figure 8 CMy of configuration Front/Rear 30°/60° (left) and 60°/30° (right) at Mach 0.5, with the dashed line showing the 10° roll deflection.

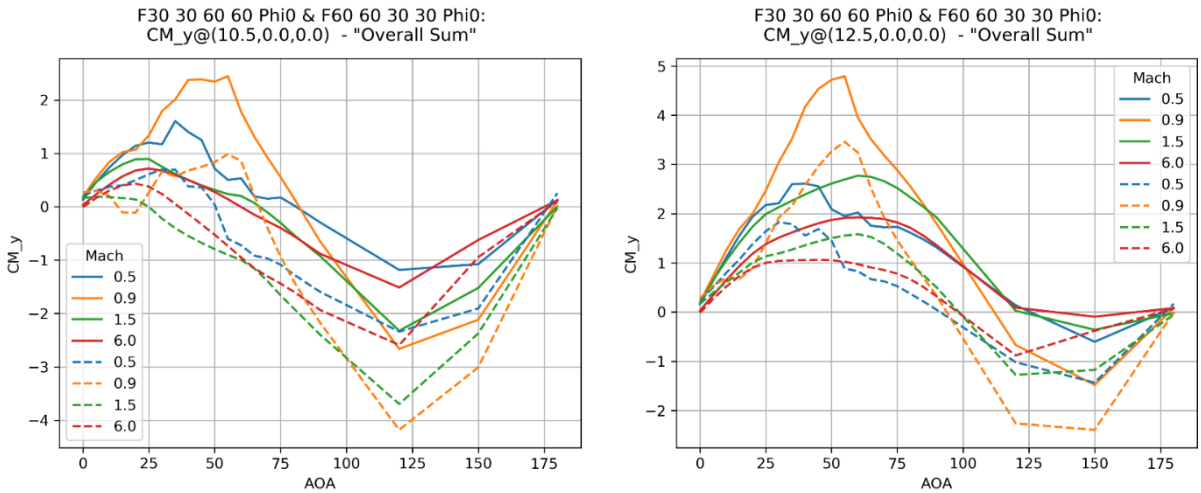

Figure 9 CMy of configuration Front/Rear 30°/60° (solid line) and 60°/30° (dashed line) for multiple Mach numbers, with a COG position of 10.5m (left side) and 12.5m (right side) from the nose of the vehicle.

Table 7 Stable and Trimmable Range, based on the expected SBD settings

Center of Gravity (COG):	10.5m	12.5m
Mach 0.5:	50° - 80°	90° - 125°
Mach 0.9:	67° - 81°	95° - 112°
Mach 1.5:	25° - 67°	98° - 120°
Mach 6.0:	35° - 60°	98° - 135°

It can be seen that the stable and trimmable condition is highly dependent on the COG position.

3.5 Aerothermal Database (ATDB)

RANS calculations, performed with the DLR flow solver TAU, are the base for the calculation of the structural heating of the rocket. Therefore, the surface heat flux is calculated for characteristic flight conditions along the thermal sizing trajectory, which was generated in the course of the project.

3.6 Numerical Setup

The turbulence is modelled by the one equation Spalart-Allmaras eddy viscosity model. More precisely, a simplified model is used without the “ft2”-term, which results in missing suppression of turbulence in laminar regions [3]. Furthermore, the convection scheme AUSMDV is used and the gradients are reconstructed by the Green-Gauss reconstruction. The surface of the rocked is described in two different ways. First, for the evaluation of the critical hotspots on the rocket and the influence of the gas models. Therefore, the surface is defined as viscous wall where the temperature and heat flux are evaluated by the radiative equilibrium. Here, the emissivity is set to 0.8. Second, for the heat flux along the trajectory. Hereby, the surface is defined as isothermal viscous wall. Furthermore, mesh adaptation is utilized, adding 10% of new points in regions where the Mach number and pressure gradients are the highest in the flow field.
The mesh convergence study leads to an estimated error of 1.37% for the mesh used for aerothermal calculations.

3.7 Influence of the Gas Model

The influence of the gas model on the aerodynamics for high Mach numbers calculations is investigated. For that, as above described, the heat fluxes and temperatures are evaluated by the radiative equilibrium. This results in the stationary condition on the surface for an infinite long flight on one particular trajectory point. One shall remember, that radiative equilibrium calculations leads to a temperature overestimation and a heat flux underestimation and is used here only for the gas model analysis. The flight condition is the one of the maximum heat flux, see Table 8.
The heat flux distribution on the luv surface of the rocket for both gas models is depicted in the Figure 10. The perfect gas model is the upper half and the equilibrium gas model is the lower half of the illustration. For the perfect gas model, the heat flux in the region of the leading edge of the front and rear flap is moderate. The equilibrium gas model shows local regions where the heat flux is increased. The increased heat flux on the fairing of the front flap, see the circled 1, is caused by the interaction of the nose shock with the shock generated by the front flap. Furthermore, the region marked with the circled 2 is affected by the compression shock generated by the flap itself. The heat flux on the rear flap is influenced by the shock originating from the rocket body. The region is marked with the circled 3. The reason for the shock interactions, seen in the calculations with the equilibrium gas model, is the reduced distance of the shock to the surface. This reduction is caused by the

energy needed for the dissociation and recombination of the gas behind the shock.
The strong influence of the gas model towards higher local heat fluxes leads to the conclusion to use the equilibrium gas model for the calculation of the aerothermal database.

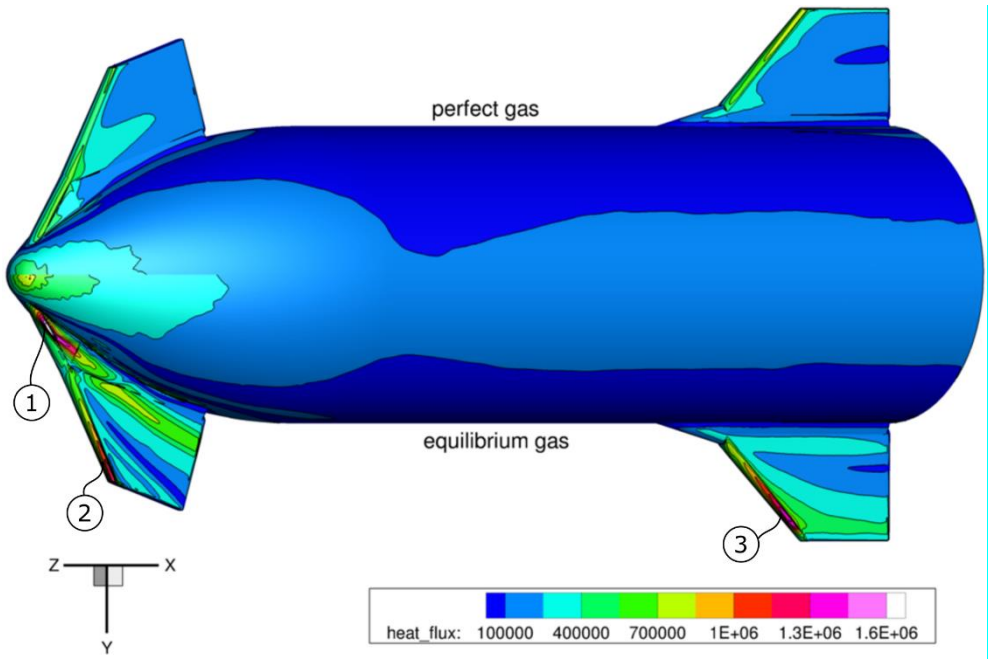

Figure 10 Comparison of the surface heat flux distribution between the perfect gas and equilibrium gas model.

3.8 Aerothermal Calculations

The aerothermal calculations are not coupled with the structural model of the rocket. Hence, a number of flight conditions along the re-entry trajectory of the rocket have to be chosen where the heat flux on the surface is calculated. The method describes in the following is based on calculations performed for a retro propulsion-assisted launch vehicle [5]. The relevant conditions are identified w.r.t. the second thermal sizing trajectory. The estimated heat flux from the trajectory calculation is depicted in Figure 11. The local extrema are named with numbers. The filled circles mark the flight conditions RANS calculation are performed for. The heat fluxes for the empty circles are "synthetic" heat fluxes. They are scaled with the flight conditions from the source and target flight point. The time of flight, rocket velocity and the gas condition for each marked point are listed in the Table 8. The scaling is done

by the following equation [5]

$$q_{target} = q_{source} \frac{\rho_{target}^{0.5} u_{target}^{3}}{\rho_{source}^{0.5} u_{source}^{3}} \quad (1)$$

The evaluation of the heat flux by the RANS calculation needs the local wall temperature. This wall temperature is unknown due to the non-coupled approach. Thus, two calculations with different isothermal wall temperatures are performed for each chosen relevant flight condition. The wall temperatures are 200K and 600K. This enables to interpolate the local heat flux by the local wall temperature.

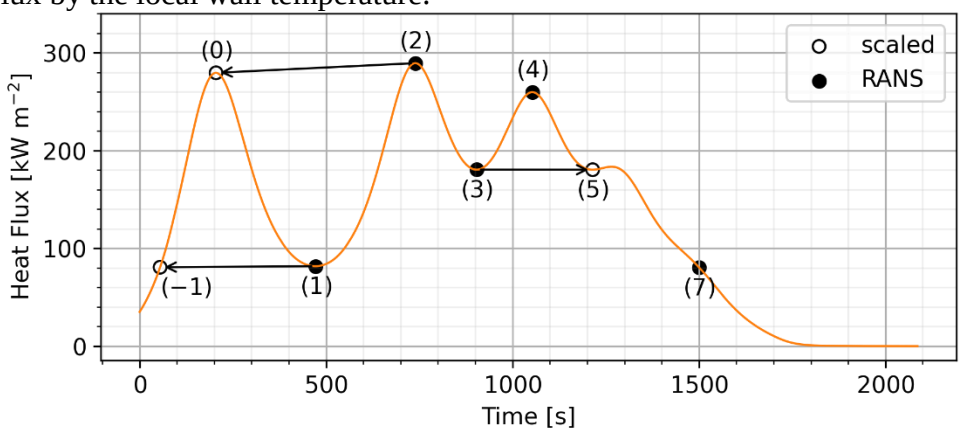

Figure 11 Available heat flux surface solution along the thermal sizing trajectory.

Table 8 Flow conditions for the available heat flux solutions.

Index	Time [s]	TAOA [°]	Velocity [m s^{-1}]	Pressure [Pa]	Density [kg m^{-3}]	Temperature [K]
-1	55	40.0	7406.2	0.1461	$2.716e-6$	186.88
0	205	40.0	7253.5	2.2085	$3.708e-5$	207.45
1	472	40.0	6982.0	0.2166	$4.033e-6$	186.87
2	739	40.0	6684.6	4.11110	$6.651e-5$	215.33
3	904	40.0	6246.7	2.36938	$3.962e-5$	208.30
4	1053	40.0	5788.8	8.71900	0.000133	229.01
5	1215	40.0	4992.0	10.8887	0.000163	233.22
7	1500	40.0	2973.8	65.7093	0.000847	270.24

The above described procedure leads to heat flux data for different times of flight and wall temperatures on a fine surface mesh. These data are interpolated via moving least-squares interpolation [6] onto the mesh needed

for the structural analysis. This results in a database of surface heat flux over time of flight and temperature. Therewith, a local heat flux can be interpolated for every time of flight and local surface temperature along the trajectory.

3.9 Further Thermal Investigations

The Figure 12 depicts the heat flux distribution on the luv surface of the rocket for the flight condition of maximum heat flux of the thermal sizing trajectory. The isothermal wall temperature is set to $200K$. Furthermore, the flaps are deflected as planned for the flight at this trajectory position. It can be seen, the heat flux hotspot in the leading-edge region of the belly fairing of the front flap remains high despite the deflection of the flap due to interaction with the nose shock. The heat flux on the front flap itself is lower as the flap is further inside the shock of the body of the rocket. Moreover, the rear flap is inside the body shock and thus the heat flux peak on the leading edge does not appear. Consequently, the front fairings need to be considered as the part of the rocket with the highest thermal load.

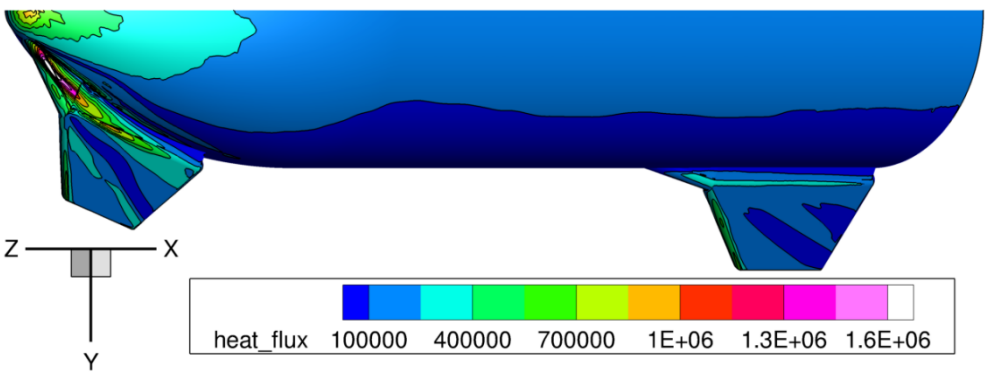

Figure 12 Heat flux distribution on the luv surface with an isothermal wall temperature of $200K$ for the flow condition of the maximum heat flux of the thermal sizing trajectory and deflected flaps.

3.10 Usage of the ATDB

The ATDB spans a two-dimensional matrix of heat fluxes over every surface point. The dimensions are the time of flight and the surface temperature. This enables to interpolate bi-linearly between the dimensions. Thus, the heat flux can be calculated as function of the local surface temperature and the time of the flight. The structure is modelled as lumped mass. Hence, the heat flux affects the total surface elements volume without considering heat conduction. Integrating the individual heat fluxes over the time of flight lead to the temperature prediction. The assumed material properties are based on

CC-SiC, developed by DLR in Stuttgart. The results are used for sizing of the thermal protection shield (TPS) of the upper stage.
The Figure 13 shows the temperature distribution of the front flap and the luv side of the body at the first heat flux peak along the trajectory at $t = 218$s. The leading-edge region of the front flap fairing shows locally the highest temperatures up to 2700K. The gradients of the temperature distribution on the luv side of the body are smaller and the maximum temperature is located at the nose of the rocket with approximately 1800K.

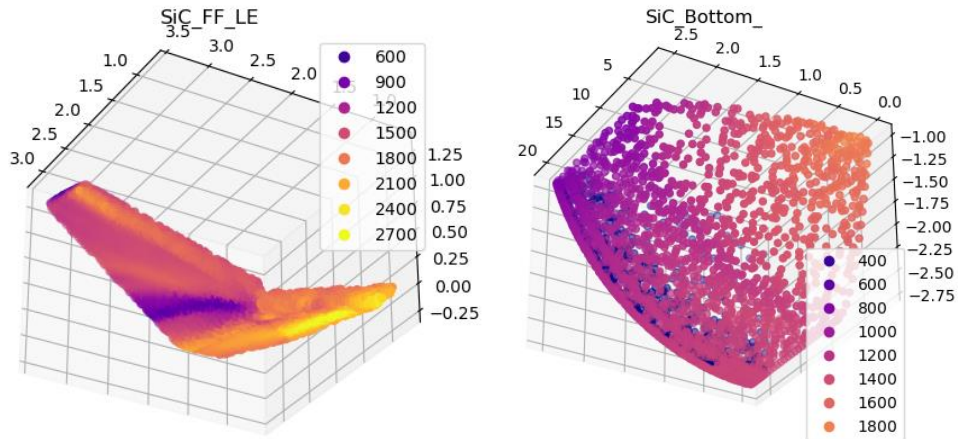

Figure 13 Temperature distribution at the first heat flux peak along the trajectory for the front flap (left) and the luv side of the body (right).

The heating of the open engine bay is approximated by heat fluxes derived from the literature. The convective heat flux due to hot gases during the retro-propulsion phase are approximated by a comparable rocked configuration with 100kWm^{-2} [7]. The radiation heat flux is conservatively approximated by the measured heat flux of a kerosene and liquid oxygen propelled rocked during firing on ground [8]. The maximum measured heat flux is approximately 50kWm^{-2}. This results in a total heat flux of 150kWm^{-2}.
The Figure 14 depicts the temperature evolution in the engine bay during the descent phase (upper) and the retro-propulsion phase (lower) for aluminum (left) and cork (right), assuming a TPS thickness of 5mm (no recession considered). The retro propulsion maneuver takes the final descent state of the average cork temperature (350K), see the upper right graph in Figure 14 , as temperature input and assumes a uniform heat flux of 150kWm^{-2}. This results in final temperatures of approximately 450K for aluminum and 500K for cork after retro-propulsion.

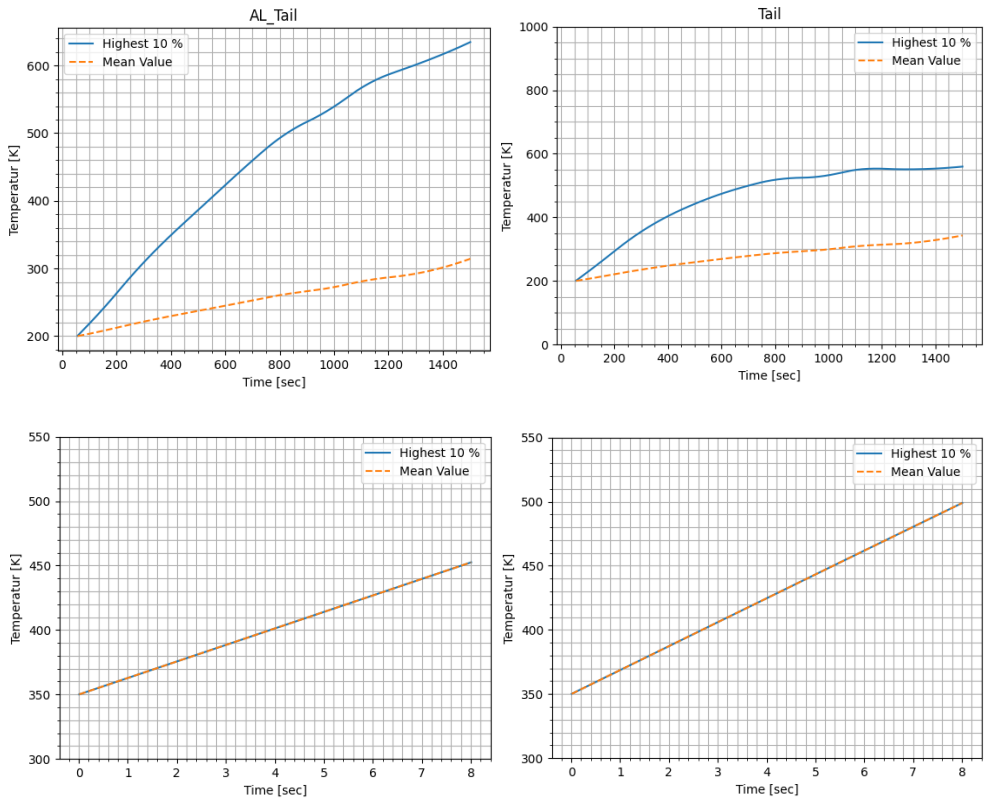

Figure 14 Temperature evolution in the engine bay during descent phase (upper) and the retro-propulsion phase (lower) for aluminum (left) and cork (right).

4 Supersonic Wind Tunnel Tests

4.1 Tri-sonic Wind Tunnel

TMK at DLR Cologne is a trisonic blow down wind tunnel with a rectangular test section of 0.6 m x 0.6 m, sketched in Figure 15. Air from a pressure reservoir of up to 60 bar passes storage heater and settling chamber (diameter 2.2 m) to enter an adaptable Laval nozzle. The wind tunnel model in the following test section is usually fixed via sting to the motion control device which allows for an alteration of the incidence angle α. Thereby, during one test investigations at different Mach numbers for certain angle of incidence ranges can be performed. A large pressure reservoir allows for a maximum testing time depending on Mach and Reynolds number of up to 60 seconds.

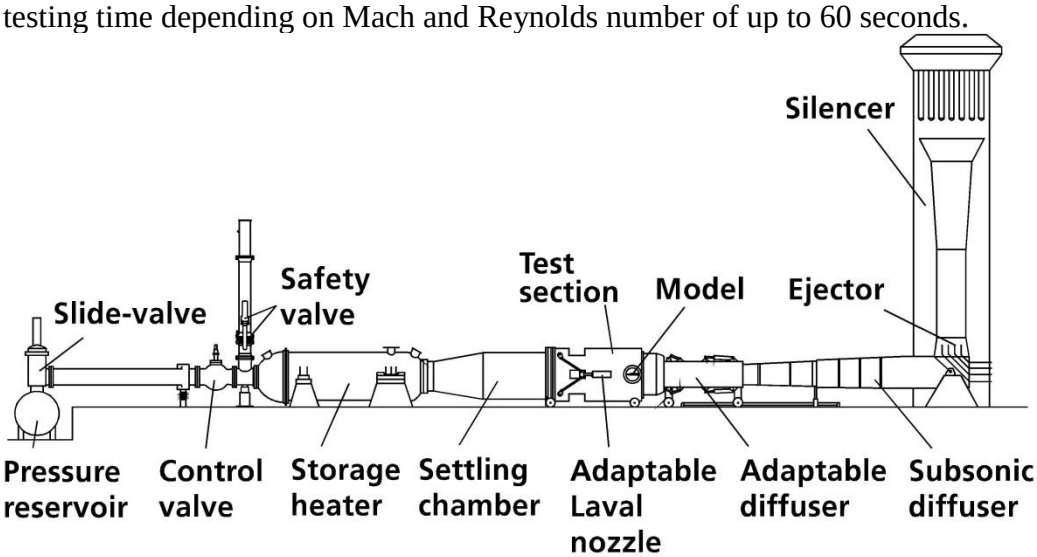

Figure 15: Schematic of Trisonic Wind Tunnel TMK

Standard Mach number range is between 1.25 and 4.5. The wind tunnel is operated at a static pressure of one bar for Mach numbers smaller than 1.2 and at a dynamic pressure of one bar for Mach numbers greater than 1.2. Mach numbers up to 5.7 can be reached by heating the flow in the storage heater and ejecting additional mass flow downstream of the subsonic diffuser. For Mach numbers below 1.2 an additional transonic test section with perforated walls is installed downstream of the supersonic test section. In dependence of the flow conditions the relative aperture of the perforation is varied to ensure adapted boundary layer suction on all four side walls. As the

wind tunnel is operated at a constant static pressure slightly above the ambient pressure, dynamic pressure and Reynolds number grow with increasing Mach number. In general Mach number can be kept constant within a bandwidth of ± 0.005.

Figure 16 shows a picture of the TMK's supersonic test section (flow direction is from the left). The performance map of the facility is given in Figure 17.

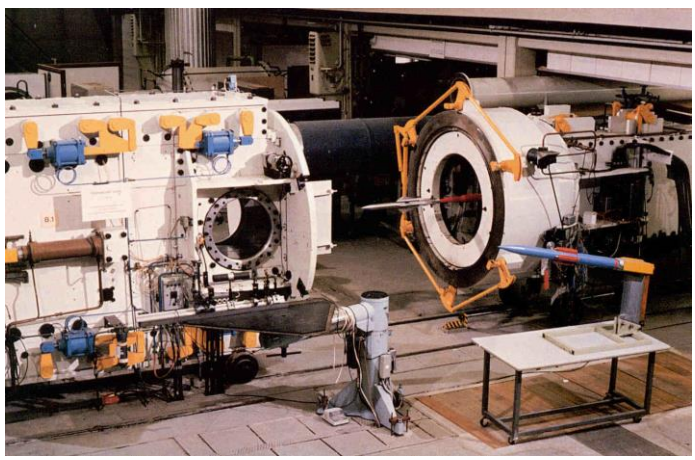

Figure 16 Trisonic Wind Tunnel TMK

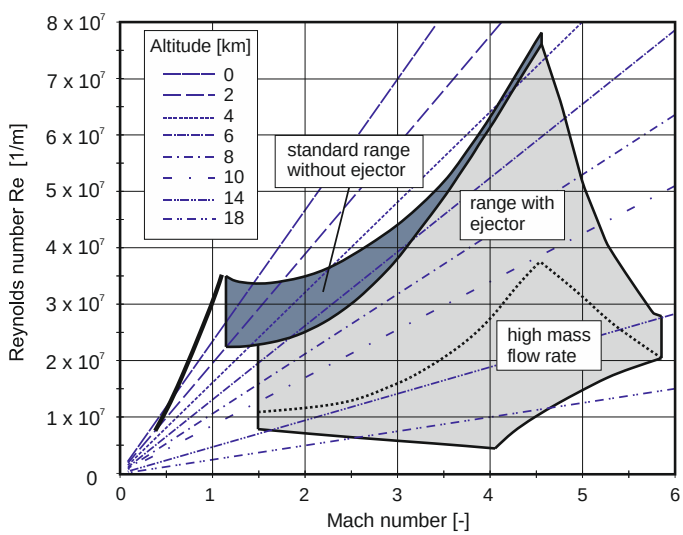

Figure 17: Performance map of Trisonic Wind Tunnel TMK

4.2 Wind Tunnel Model

Based on the reference design, a modular wind tunnel model with a scaling of $1:126{,}58 = 0.79\%$ was developed. The scaling was chosen to minimize blockage of the wind tunnel and allow for sufficient forces and moments. The design consists of a fuselage, four flaps with each five possible settings and two tail settings.

The main parameters of the wind tunnel model are:

Table 9 Wind Tunnel Model Parameters

Parameter	**Formula**	**Value [Unit]**
Reference Length	L_{ref} = Dref	0.04266 [m] = 42,66 [mm]
Reference Area	$S_{ref} = \pi * D_{ref}^2 /4$	0.0014293784 [m²] = 1429,37 mm²
Front Flap Settings		0°, 30°, 60°, 90°, stump*
Rear Flap Settings		0°, 30°, 60°, 90°, stump*
Roll Deflections		0°, 10°

* “stump” represents the case where no flap, but only the protrusion of its hinge line is present

The model is shown in Figure 18, Figure 19 and Figure 20.

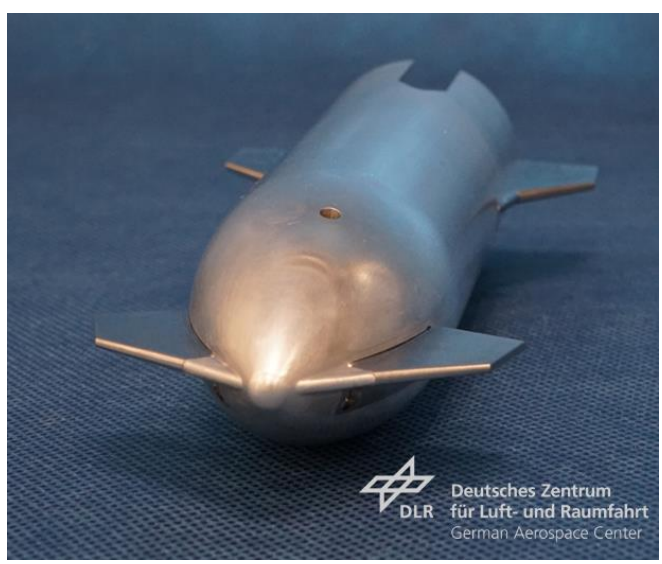

Figure 18 Frontal view

Figure 19 Right Frontal flap parts, side view

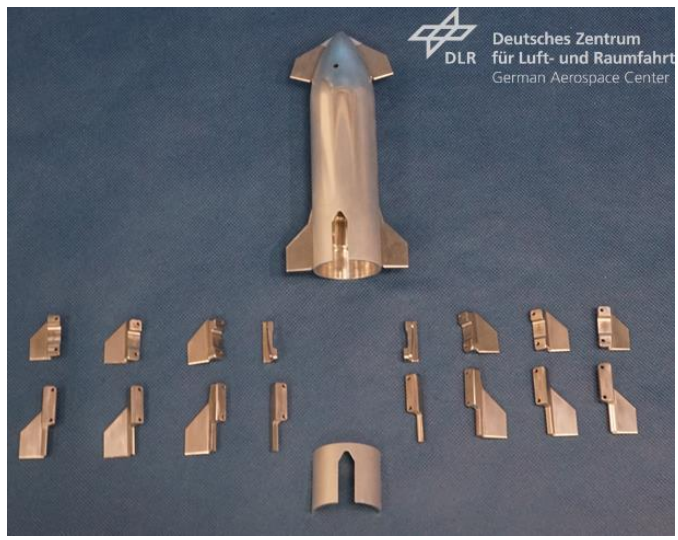

Figure 20 All Parts, top view

4.3 Model Instrumentation

A ¾ inch six-component TASK/Able balance was selected to measure aerodynamic forces and moments in the design phase. The balance was mounted onto an arm and was aligned with the x-axis of the fuselage, as shown in Figure 21. The angle between the balance and the arm amounts to 65° so that the aerodynamic influence of the arm on the model can be minimized.

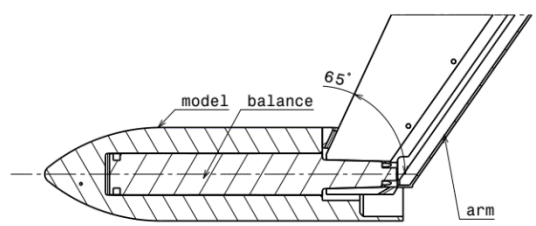

Figure 21 Installation of the wind tunnel balance

Figure 22 Installation of the wind tunnel balance

The uncertainties of the balance depend on the load applied to it. Never the less, in this report two standard deviations of the residuals (95% confidence interval) from the calibration data is taken as uncertainties for the calculation of the error bars.
Furthermore, two Kulite sensors were used to measure the model base pressure between 0 and 17 bar.

4.4 Data Post Processing

Data of the balance and of all sensors were recorded simultaneously with an acquisition rate of 200Hz. Post-processing was performed after the test with an in-house tool. The data was filtered forward-backward with a Gaussian filter, so that no phase distortion occurred. Figure 23 shows the filter properties. It features a constant phase of zero, smooth roll-off and a cut-off frequency of 1 Hz. Figure 25 gives an example of the raw and the filtered coefficients as a function of AoA.

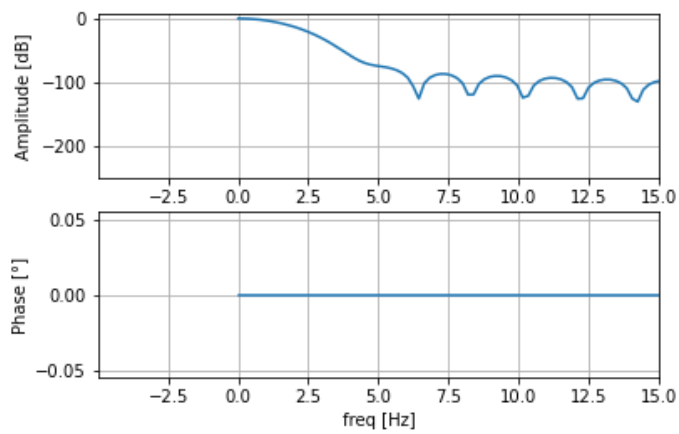

Figure 23 Filter properties

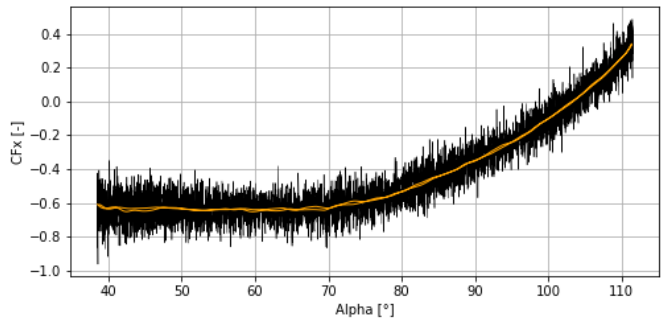

Figure 24 Raw and filtered coefficients as a function of AoA, run Nr = 23, Ma = 3.0, model = ”Stump”, CFx

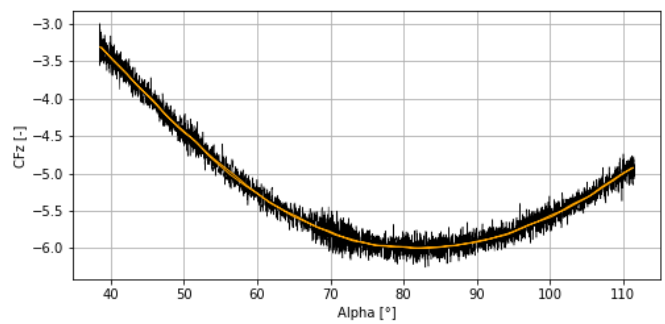

Figure 25 Raw and filtered coefficients as a function of AoA, run Nr = 23, Ma = 3.0, model = ”Stump”, CFz

4.5 Wind Tunnel Tests

The available flap settings (see Table 9) were tested in different combinations according, whereas Table 10 gives the used naming convention.

Table 10 Naming Convention of Configurations

	Naming convention	**Example**
Symmetric case	F/R <Flaps front>°/<Flaps rear>°	F/R 30°/60°
Asymmetric case	F/R <Flap 1>° <Flap 2>°/<Flap 3>° <Flap 4>°	F/R 0° 30°/ 0° 0°
No flaps	“n” is used for stumps/ no flaps	F/R n n/0° 0°

4.6 Angle of Attack Range and Roll Deflection

The range of the possible Angle of Attack region is limited by the wind tunnel parts and their setup. Following ranges were used during the tests:

- -30° – +50°
- +40° – +120°.

The second AoA range implies a critical condition at the start-up of the wind tunnel, due to the large initial AoA value of about 40°. Thus, initial tests were performed within the lower range, namely from -30° to +50°, incorporating a 0° AoA setting. A gradual assessment from the zero-position enabled checking of the balance's forces and moments, ensuring the balance is operated within its limitations. A startup condition of 40° was reached and deemed to be acceptable, giving a go for the higher AoA range.

The test matrix is divided in two sections, one without a roll angle and one with a 10° roll angle. The rotation is applied between the balance and the model, thus around the model's x-axis. Thus, the tests were conducted with a constant roll angle, whereas the sideslip angle changes during the Angle of Attack sweep.

4.7 Test Matrix

The Test matrix is based on the preliminary test plan. It is grouped into force and moment measurements (Table 11) as well as oil film pictures (Table 12) and schlieren generation (Table 13).

Table 11 Test Matrix of the Wind Tunnel Tests

No.	Flap deflection angle [°]				Alpha [°]	Roll [°]	Mach	Test focus/ description
	Left-front	Right-front	Left-rear	Right-rear				
0	0	0	0	0	-10 – +50	0	1.5, 2, 3	Force allowance verification
1	None	None	None	None	40 – 110	0	1.5, 2, 3	Effect of Fuselage
2	0	0	None	None	40 – 110	0	1.5, 2, 3	Effect of Front Flaps
3	None	None	0	0	40 – 110	0	1.5, 2, 3	Effect of Rear Flaps
4	0	0	0	0	40 – 110	0	1.5, 1,6, 2, 3	No Deflection
5	30	30	0	0	40 – 110	0	2, 3	Front Deflection
6	60	60	0	0	40 – 110	0	2, 3	
7	90	90	0	0	40 – 110	0	1.5, 2, 3	
8	0	0	30	30	40 – 110	0	1.5, 2, 3	Rear Deflection
9	0	0	60	60	40 – 110	0	1.5, 2, 3	
10	0	0	90	90	40 – 110	0	1.5, 2, 3	

11	30	30	60	60	40 – 110	0	1.5, 2, 3	Flight & Trim relevant cases
12	60	60	30	30	40 – 110	0	1.5, 2, 3	
13	0	30	0	0	40 – 110	0	2, 3	Asymmetry of Front Flaps
14	0	60	0	0	40 – 110	0	2, 3	
15	0	90	0	0	40 – 110	0	2, 3	
16	0	0	0	30	40 – 110	0	1.5, 2, 3	Asymmetry of Rear Flaps
17	0	0	0	60	40 – 110	0	2, 3	
18	0	0	0	90	40 – 110	0	2, 3	
19	90	90	90	90	40 – 110	0	1.5	Maximum Deflection
20	0	0	0	0	40 – 110	10	2, 3	No Deflection
21	0	30	0	0	40 – 110	10	2, 3	Asymmetry of Front Flaps
22	0	0	0	30	40 – 110	10	2, 3	Asymmetry of Rear Flaps
23	0	0	0	60	40 – 110	10	2, 3	
24	90	90	90	90	40 – 110	10	2, 3	Max. Deflection, Effect on Roll Moment
25	30	30	60	60	40 – 110	10	2, 3	Flight % Trim relevant case

Furthermore, a map can be extracted from the test matrix, showing the model configurations for the investigation of the longitudinal stability, summarized in Figure 26. From these data points a meaningful prediction of the functionality of the flaps can be made.

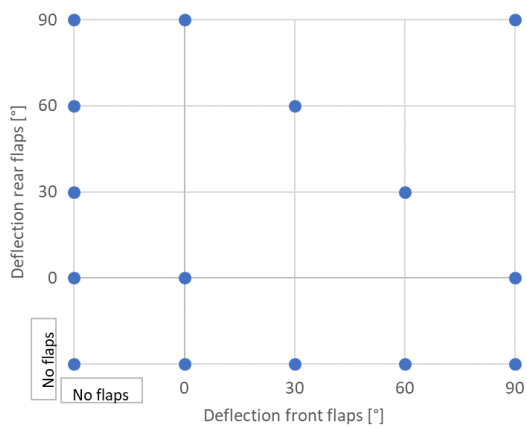

Figure 26 Model configurations for the investigation of the longitudinal stability

4.8 Results

4.9 Repeatability of the Test

Two runs, one from the lower and one from the higher AoA range were compared with each other, giving an indication of the repeatability as they have an overlapping AoA range from 38° to 50°.
The comparison results for the configuration of “0°/0°/0°/0°” (all the four

flaps were set at 0°) at a Mach number of 3 are given in Figure 30, showing a very good repeatability.

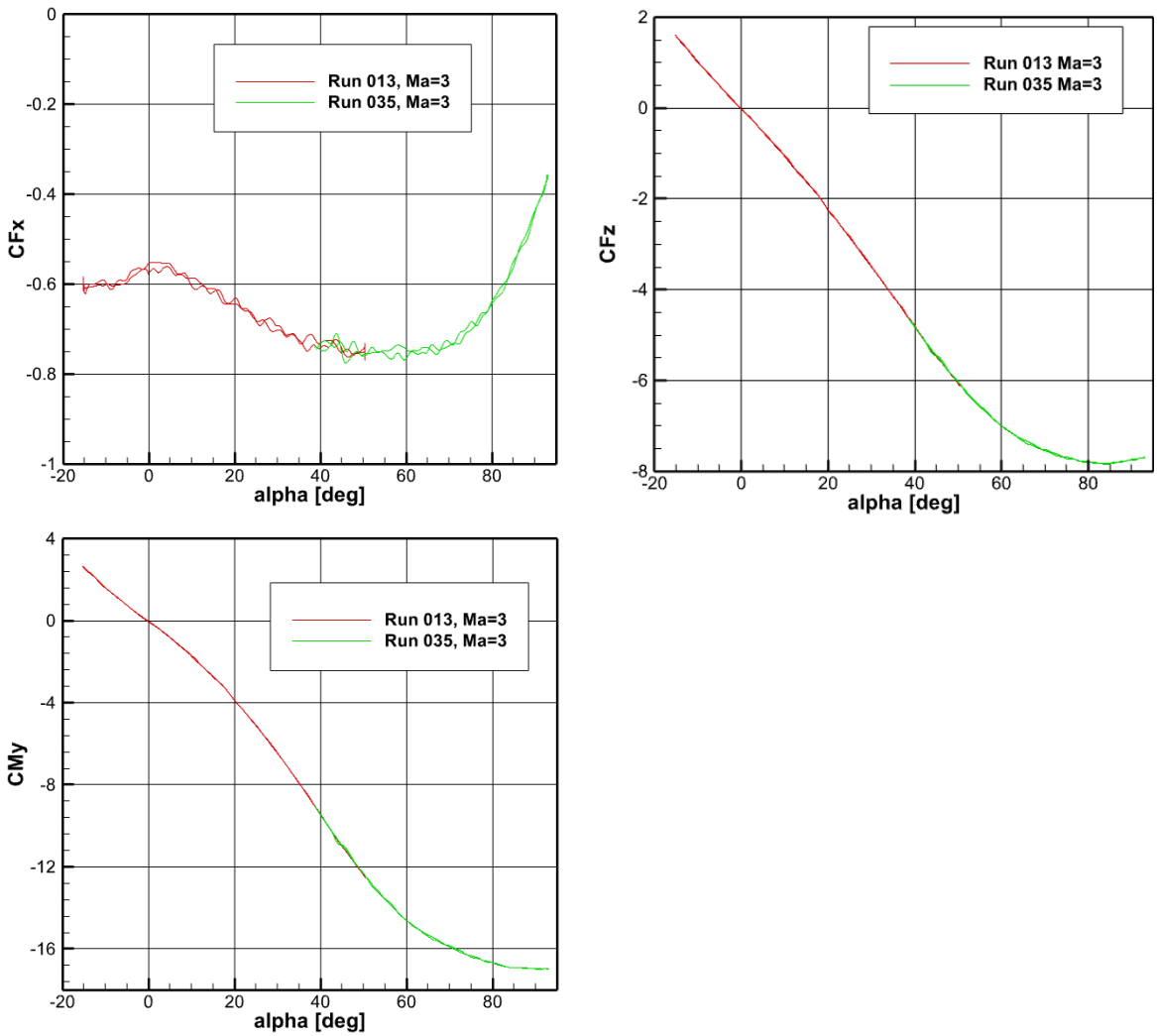

Figure 27 Repeatability of the test, model configuration="0°/0°/0°/0°", Ma=3

4.10 Force and Moment Evaluation

Within this section, some key results of the Wind Tunnel Tests are shown using three graphics per configuration:

- Force coefficient plots
- Moment coefficient plots
- Pressure coefficient plots
    - Based on the two pressure sensors
    - The line is based on the average of the two sensors, whereas the border of the shadowed area indicates the individual sensor data

  Whereas each configuration plot shows all available Mach numbers and also the CFD results where available.

The origin is at the nose (x=0), the x-axis points from the nose to the base, the z-axis to the top and y follows the right-hand rule.

Meaning of uncertainty bars:
All experimental lines have uncertainties bars plotted with them. It shall be pointed out that they indicate measurement (equipment) uncertainties only, not systematic uncertainties.

Meaning of shading in the plots:
The shadowed area of the CFD results represents the values with a ±10% range of its value. The minimum value is 2% of the maximum value of the measurement. For the CP plots, the shading rim indicates the pressure sensor readings, whereas the displayed line is the average data of it.

The aerodynamic database and the performed calculations and configurations are described in section 3.1.

Figure 28 and Figure 29 show the CFD-Wind Tunnel Test comparison for the most relevant flight condition of F/R 30°/60° and 60°/30°.

F/R 30°/60°

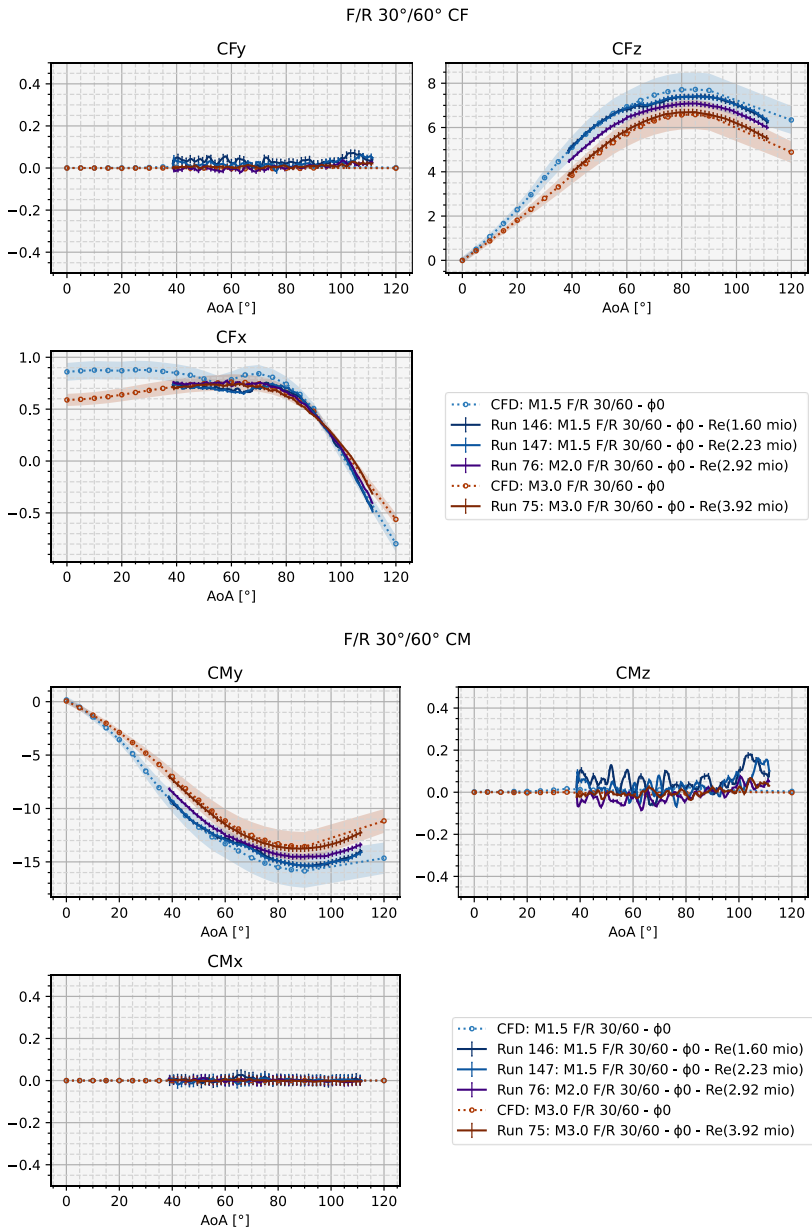

Figure 28 F/R 30°/60°, for CF and CM

F/R 60°/30°

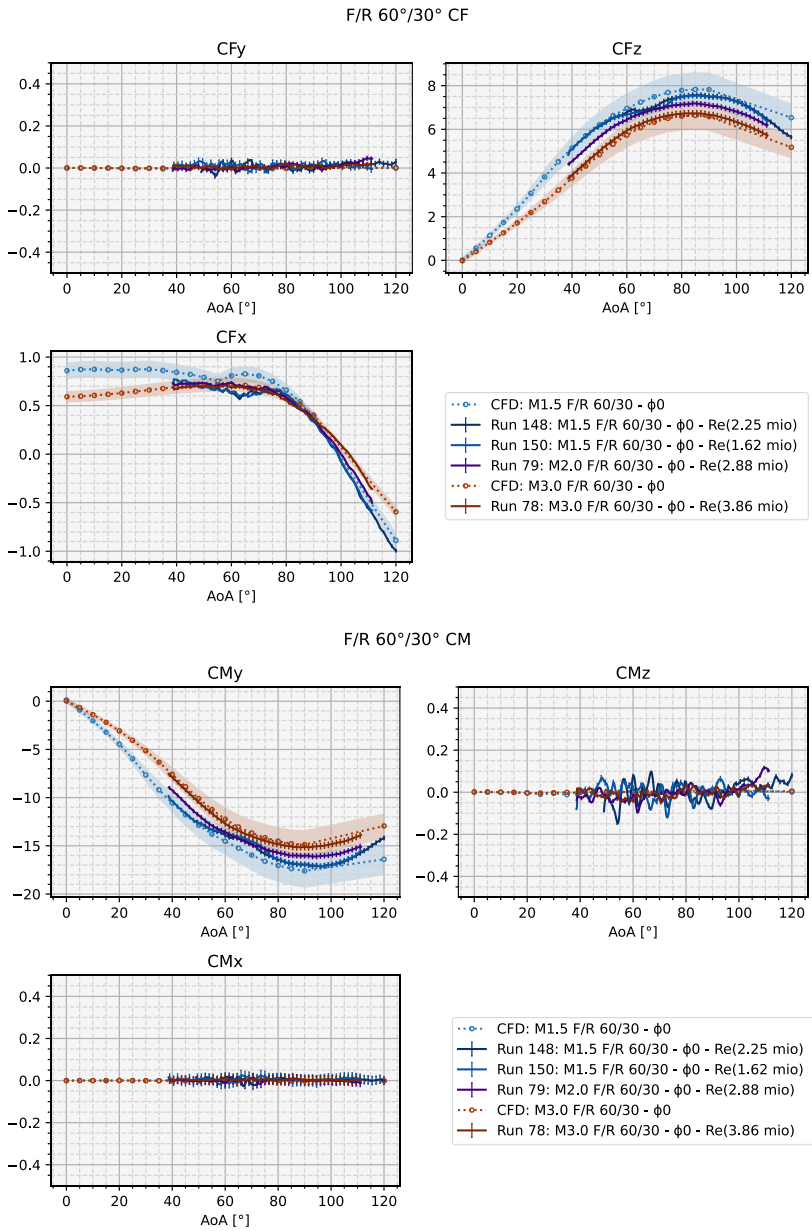

Figure 29 F/R 60°/30°, for CF and CM

4.11 Single Flap Effects – Rear Flap Effects

The effect of a change in a single rear flap (Flap 4, Rear Right) can be seen and quantified mainly as a linear function $f(\alpha)$ offset from the "no deflection" line. The effects are most prominent for CFy and CMz, CMx and with a smaller impact on CMy.

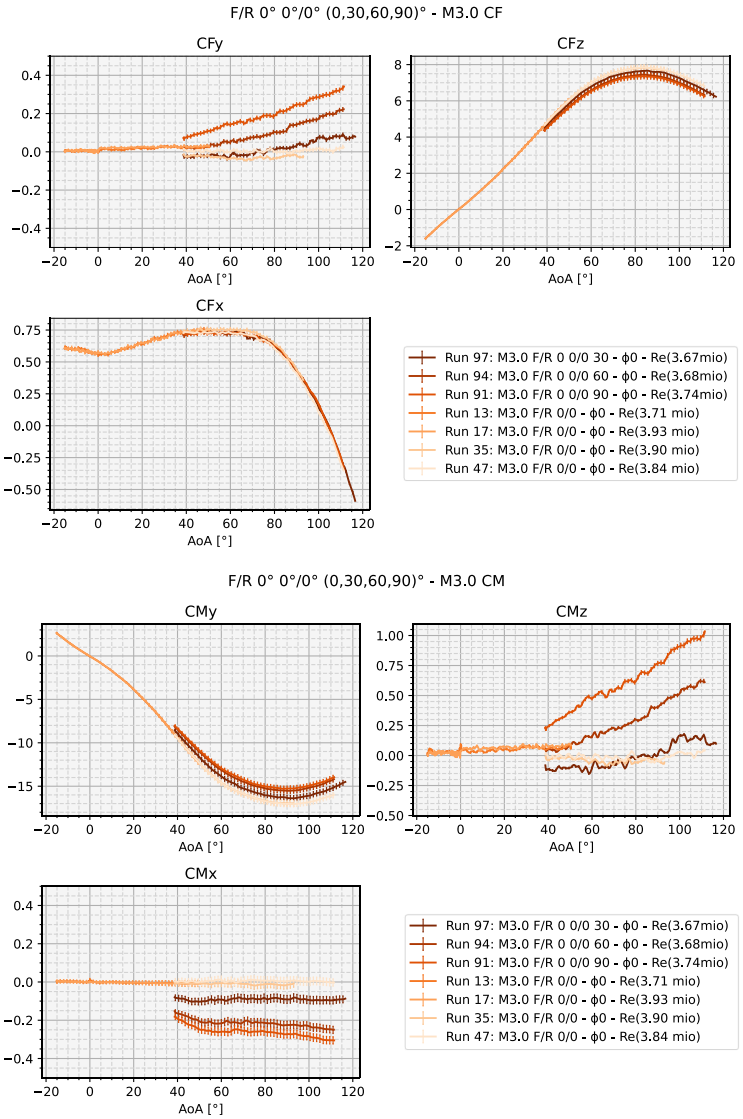

Figure 30 Single Flap Effects – Rear Flap, Force and Moment Coefficients

4.12 Single Flap Effects – Front Flap Effects

The effect of a change in a single front flap (Flap 2, Front Right) can be seen and quantified mainly as two linear functions $f_{<60°}(\alpha), f_{>60°}(\alpha)$ offset from the "no deflection" line. The effects are most prominent for CFy and CMz, CMx and with a smaller impact on CMy.

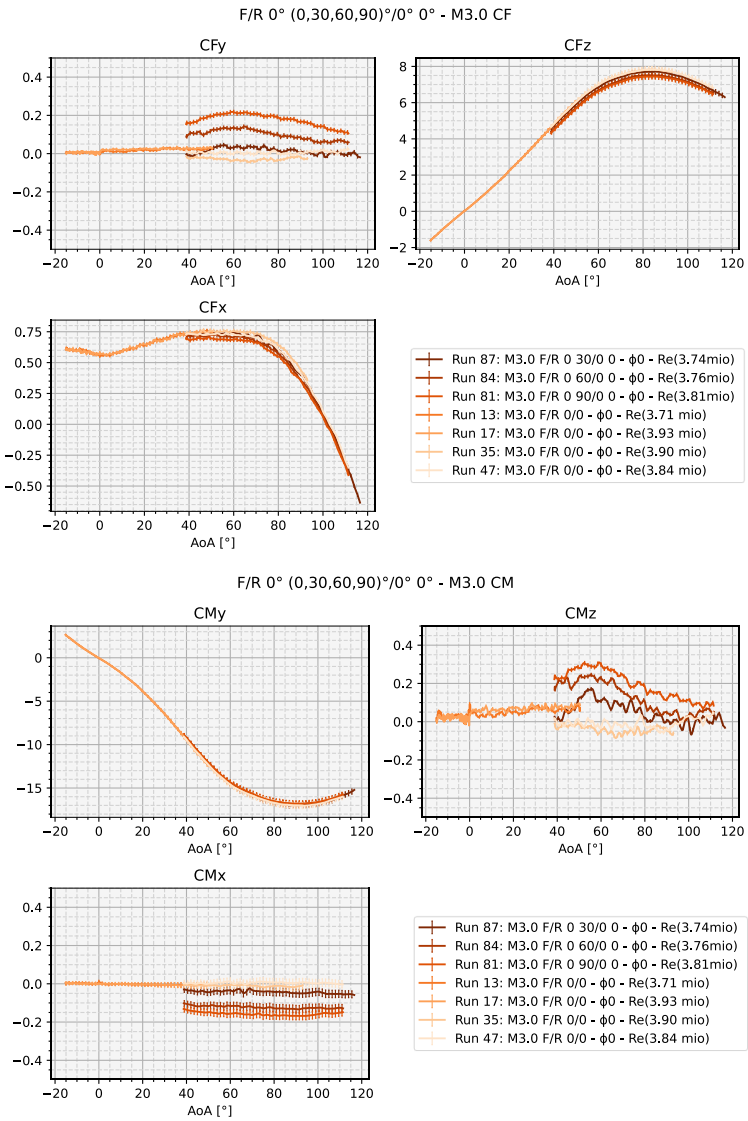

Figure 31 Single Flap Effects – Front Flap, Force and Moment Coefficients

4.13 Single Flap Effects – Front-Rear Flap Effects Comparison

When comparing the single flap effects of a front fin with a rear fin for the same deflection angle, several observations can be made:
Side Force Coefficient (Figure 32)

- For a 30° deflection, no significant change is observed
- For a 60° deflection, a separation point at approximately 85° is present, above which the lines start to separate
- For a 90° deflection, the separation point clarified at 80° to 85° with a noticable separation.

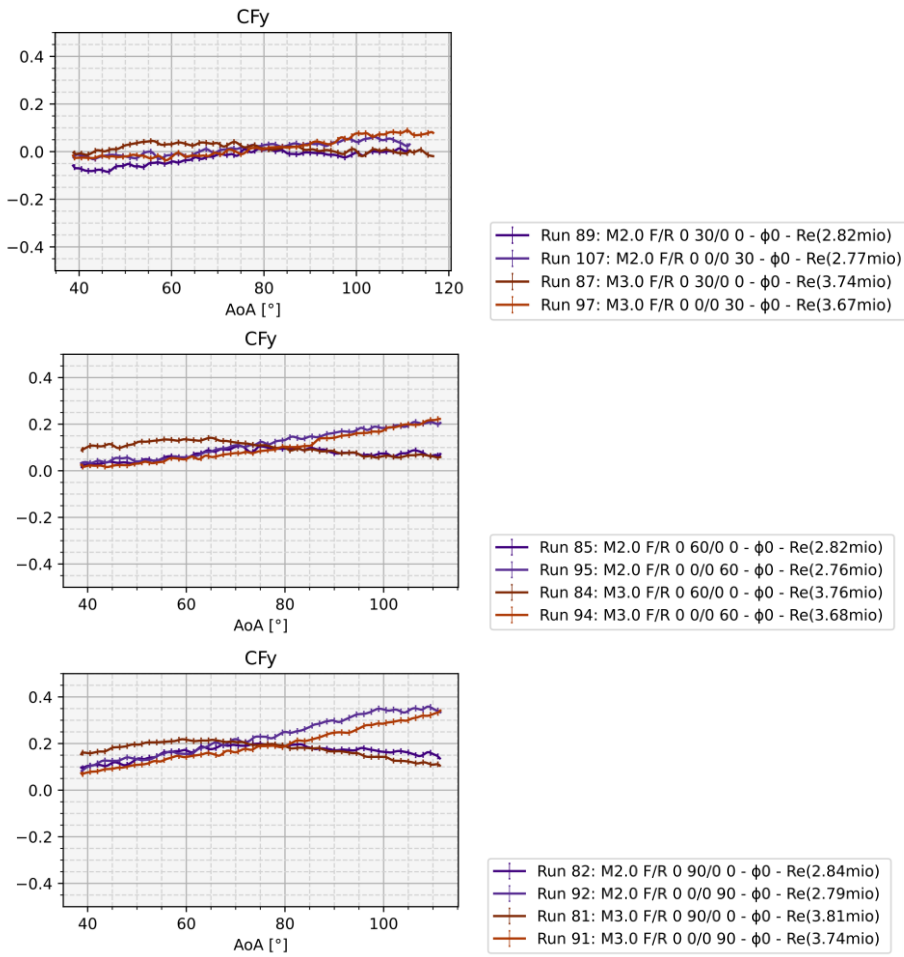

Figure 32 Single Flap Effects Comparison between front and rear flaps, 30° (top), 60° (middle), 90° (bottom), for Mach 2 and Mach 3 for the Side Force Coefficient

Yaw Moment Coefficient (Figure 33)

- For a 30° deflection, no significant change is observed
- For a 60° deflection, a separation point is visible at 65° to 70°, above which the lines strongly separate
- For a 90° deflection, the separation point moves a smaller values of 50° above which the lines separate greatly (compare scales!)

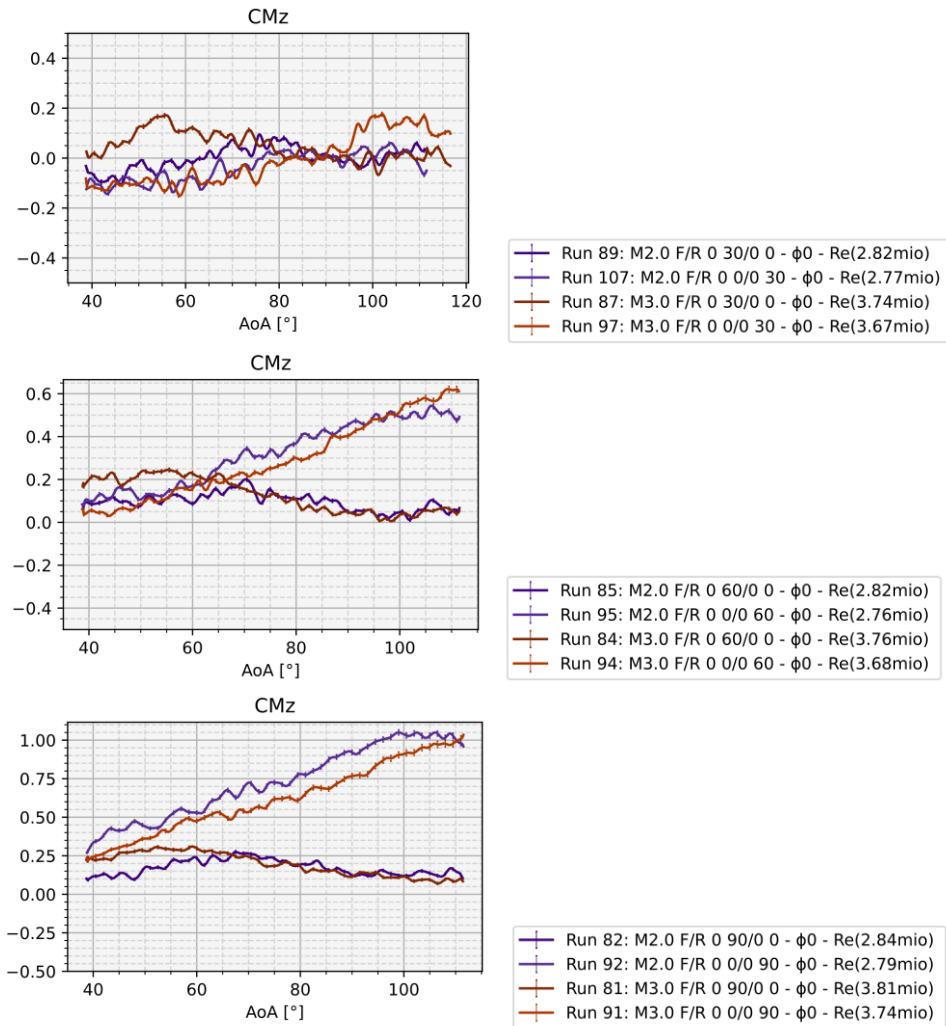

Figure 33 Single Flap Effects Comparison between front and rear flaps, 30° (top), 60° (middle), 90° (bottom), for Mach 2 and Mach 3 for the Yawing Moment Coefficient

4.14 Unsteady Flow at Lower Supersonic Mach Numbers

During the wind tunnel test unsteady flow was observed at lower Mach numbers. In order to analyze this unsteady flow phenomenon, the following key features of the measured raw Fx-, Fz- and My-component were calculated:

- Rolling standard deviation with a window length of 64 (0.32s)
- Rolling peak power spectrum with a window length of 256 (1.28s)

The first parameter indicates the overall strength of the oscillation. The second parameter gives a hint whether the oscillation concentrates at some frequencies.

Figure 34 and Figure 35 show the oscillation features of the axial force, normal force and pitching moment of the model configuration “0°/0°/0°/0°” at Mach numbers of 3, 2 and 1.5, respectively. A strong oscillation occurred in X-direction at AoA between 40° and 46° at Mach number of 1.5. In fact, the frequency of the oscillation was about 60Hz. The oscillations at higher Mach numbers and in other directions were not significant. The reason for this phenomenon needs to be investigated further, but flow separation is assumed.

The mentioned unsteady flow effects while testing at Mach 1.5 caused a force/ moment overload of the balance. To continue testing without the risk of damaging the measurement balance, the strain gauge balance was exchanged to one with higher allowable forces and moments. First tests still showed an overload condition for Mach 1.5. Through the additionally usage of the ejector, the dynamic pressure was decreased and thus the absolute values of the forces and moments, which allowed further testing without problems.

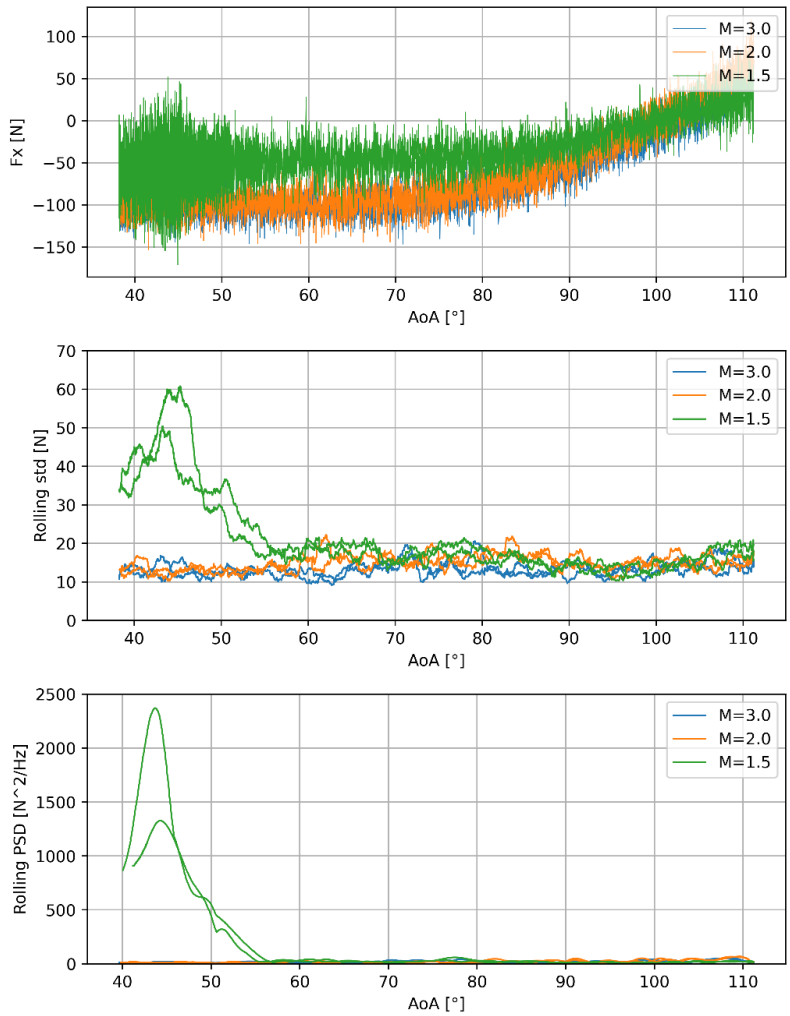

Figure 34 Oscillation characteristics of the axial force of the model configuration “0°/0°/0°/0°”

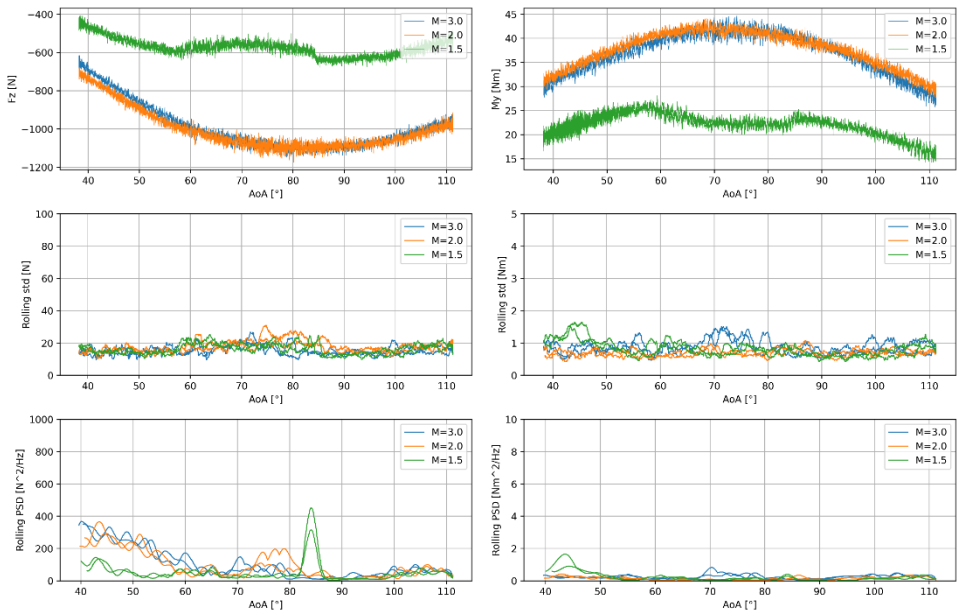

Figure 35 Oscillation characteristics of the normal force (left) and pitching moment (right) of the model configuration "0°/0°/0°/0°"

4.15 Reynolds Number Effects

As mentioned in 4.14 "Unsteady Flow at Lower Supersonic Mach Numbers" above, the Mach 1.5 experiments required the usage of the ejector. The ejector decreases the dynamic pressure and henceforth also the Reynolds number, which is shown in Figure 36. The blue line indicates the flight Re numbers, the red dots the Re number for the 3 Mach numbers without ejector, and the 3 green dots for the Mach 1.5 tests with ejector on.

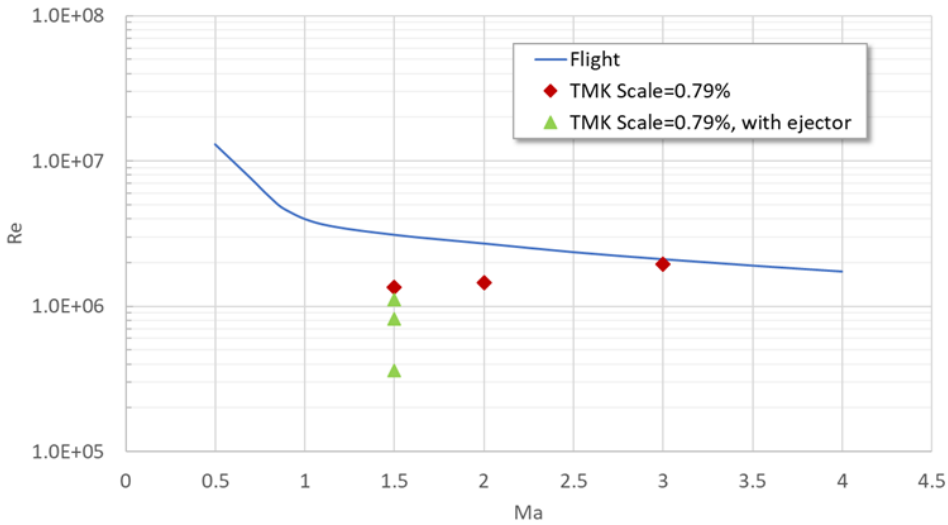

Figure 36 Reynolds numbers of flight and wind tunnel experiments

When comparing now the wind tunnel experiments to the CFD data (Figure 37 and Figure 38), one finds a significant drop in the coefficients of CFz, CFx and CMy for AoA between 55° and 90°. However, this drop is only present for the tests with the ejector on, leading to the conclusion of Reynolds number effects.

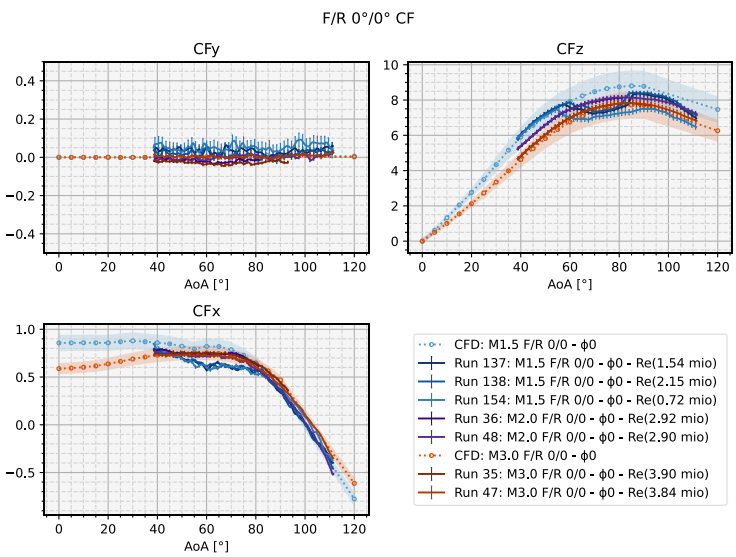

Figure 37 CFD - Wind Tunnel Comparison for F/R 0°/0°, Force Coefficients

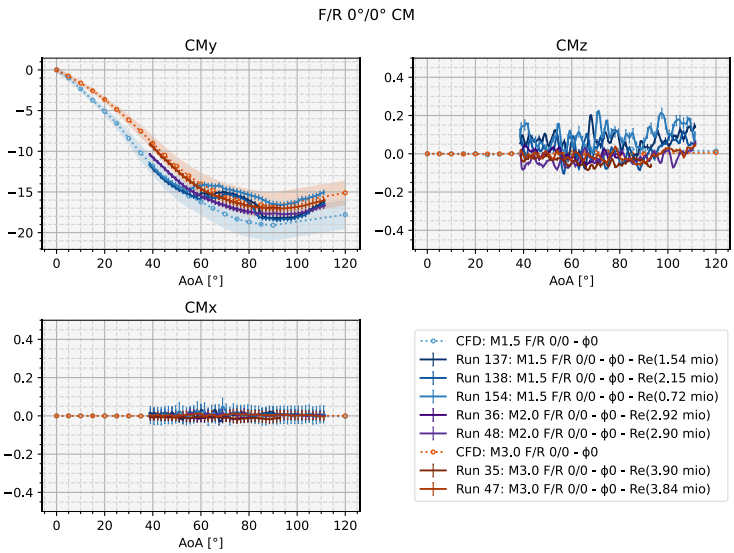

Figure 38 CFD - Wind Tunnel Comparison for F/R 0°/0°, Moment Coefficients

It is interesting to observe that this effect is most pronounced for the configuration of F/R 0°/0° (Figure 37, Figure 38), all flaps spread out completely. When taking a look at the most relevant flight configurations of F/R 60°/30° and 30°/60°, the drop is smaller (Figure 39). Additionally, it appears that the drop is even less dominant if the rear flap is retraced more and the front frap less, than vice versa.

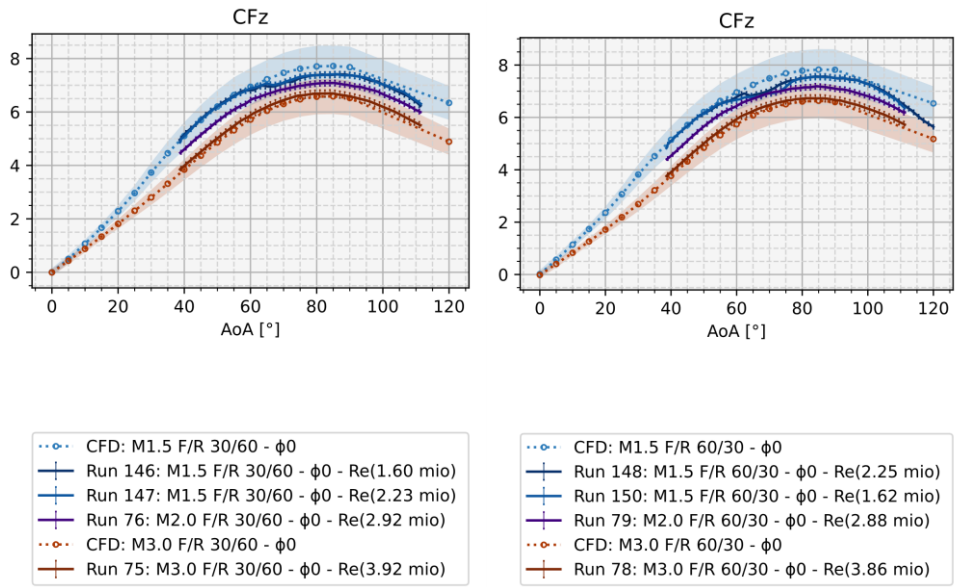

Figure 39 CFD - Wind Tunnel Comparison for F/R 30°/60° (left) and 60°/30° (right), Force Coefficients

It needs to be analyzed further, in which regard this behavior is linked to the observed unsteady flow effects in the lower AoA range described in section 4.14 above.

4.16 Superimposition Evaluation with CFD comparison

It was analyzed, in which way superimposition can be used to model the overall vehicle aerodynamics by the extraction of flap effects and their superimposition onto the fuselage aerodynamics. If this principle shows to be a valid methodology, the aerodynamic modelling effort can be reduced greatly. In theory, this should be possible for super and hypersonic flows, since the configuration flies at high Angles of Attack and a Front-Rear-Flap interaction can be assumed to be negligible.

Taking a closer look into this assumption and methodology, it was found that it is only partly applicable for certain coefficients, but not all in general. The longitudinal coefficients of CN, CA and CMy showed a good agreement, with a relative error smaller than 10% between superimposition and wind tunnel test. For the lateral coefficients, there results were also good for the supersonics regime. It was found that it cannot be used within the subsonic

regime. [2]

4.17 Oil Film

For oil film pictures, the model is “painted” with fluorescent powder and liquid medium. The model is then moved to desired AoA and started at this position. Force measurements cannot be performed at the same time, as no balance is used during oil film measurements.

Table 12 Test Matrix for oil film generation

Mach	Alpha	Roll [°]	Flap front left [°]	Flap front right [°]	Flap rear left [°]	Flap rear right [°]
Oil Film Tests, no force measurement						
1.5	70°	0	0	0	0	0
1.5	70°	0	0	30	0	30
1.5	70°	0	0	0	0	0
2	70°	0	0	0	0	0
1.5	70°	0	30	30	30	30

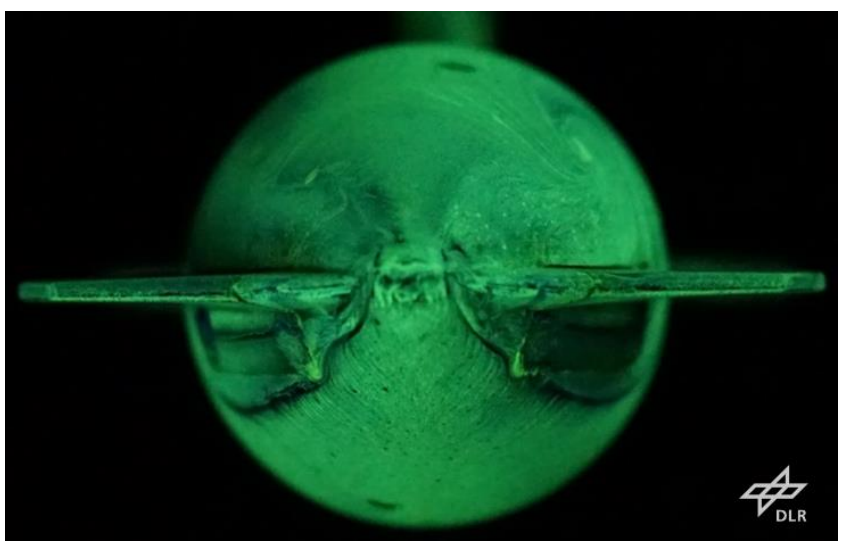

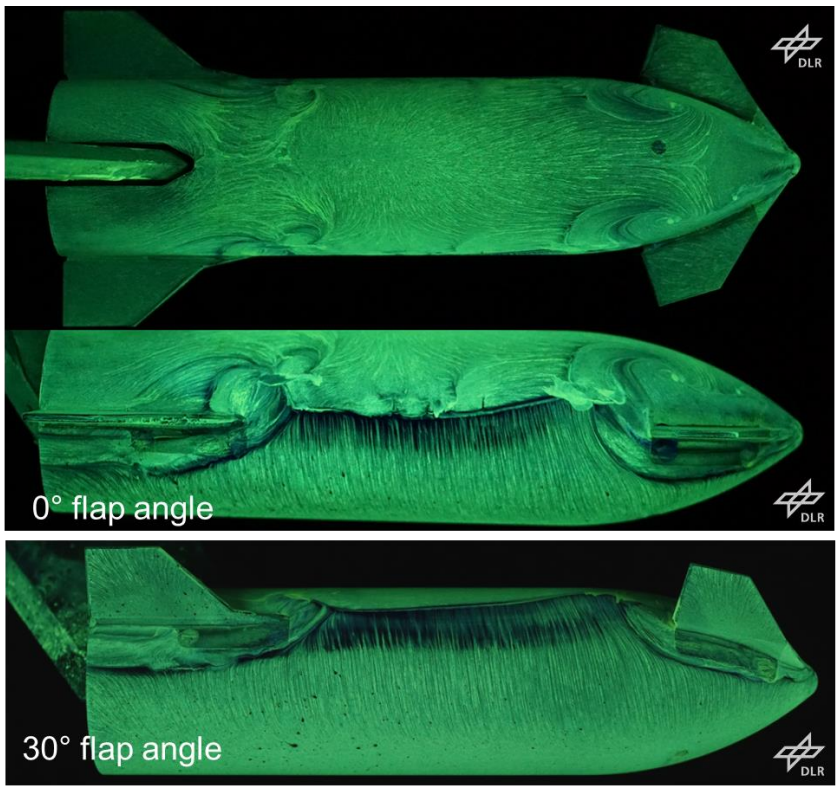

Figure 40 Oil Film pictures, for AoA 70°, Mach 1.5, front view and 0° flap view (case 1), 30° flap view (case 5, incl. ejector)

4.18 Schlieren

Table 13 Test Matrix for schlieren pictures (90° roll)

Mach	Alpha	Roll [°]	Flap front left [°]	Flap front right [°]	Flap rear left [°]	Flap rear right [°]
90° roll for schlieren, no force measurement						
3	0°	0	30	30	30	30
2	0°	0	30	30	30	30
1.5	0°	0	30	30	30	30
3	0°	0	0	0	0	0

2	0°	0	0	0	0	0
1.5	0°	0	0	0	0	0

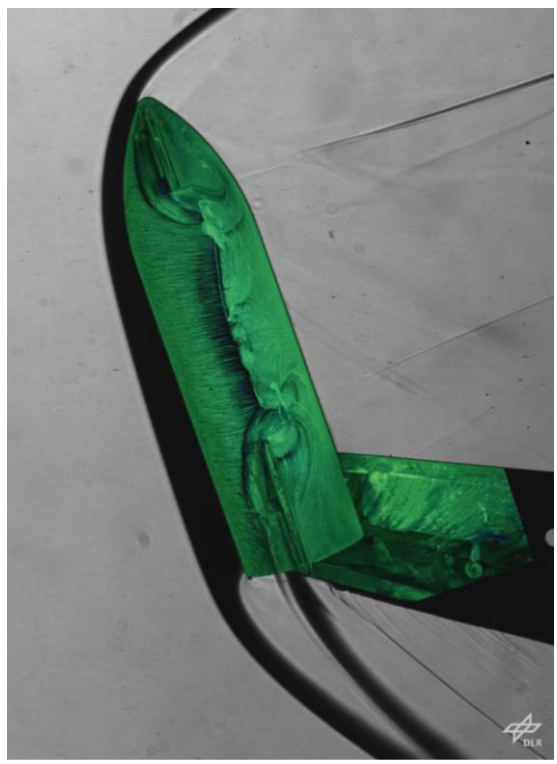

Figure 41 Schlieren Image with oil film picture (case 1) overlay for Mach 1.5 and AoA 70°

5 Summary and Project Outcomes

The ESA funded project 'RocketHandbrake' investigates the reusability of upper stages and boosters re-entering earth´s atmosphere at high angles of attack as a means for aerodynamic braking. More specifically, Supersonic Braking Devices (SBD) are used to control the vehicle during the aerodynamic descent, eliminating the need for additional Supersonic Retro Propulsion (SRP) fuel – besides the final landing burn – however, at the cost of SBD.

The concept chosen for evaluation utilizes the fuselage as a main drag generator, together with small flaps in the front and rear to provide the

required control authority. The vehicle re-enters earth's atmosphere at high angles of attack, thus requiring a suitable Thermal Protection System (TPS) for the fuselage and flaps, as well as corresponding Guidance, Navigation and Control (GNC) routines. This concept is based on the approach taken by SpaceX with their Starship launcher.

During the project, an aerodynamic database was generated and later on verified through supersonic wind tunnel tests, showing a good agreement. However, Reynold Number effects were observed, highlighting the need for further future investigation, especially within the trans- and subsonic regime. On the structural side, the flaps, the fuselage and their connection as well as actuation were designed. Initial TPS investigations for the worst-case scenario showed a feasible concept, requiring some adaptation for certain hotspots. In future iterations the thickness can likely be reduced when orientated on the reference trajectory. Currently the TPS contributes to a large part of approximately 25% to the empty vehicle mass. More precise material data and a different reference case can reduce this factor. Through mission analysis, a flyable reference trajectory as well as a thermal sizing trajectory were established, while further evaluation of the aerodynamic database allowed the definition of a permissible center of gravity (CoG) position range. Furthermore, GNC algorithms were obtained and extensively tested within the Flight Engineering Simulator (FES). The aerodynamic database assumed an initial (pre- wind tunnel tests) uncertainty of 20%, which can be reduced to approximately 10% for most cases.

To sum it up, the concept analyzed seems to be a feasible method to recover upper stages by means of aerodynamic braking and supersonic braking devices.

6 Acknowledgements

This work was performed in the frame of the ESA Project with the contract number 4000135687/21/NL/MG, with Louis Walpot as ESAs Technical Project Manager, which I want to thank for his work and support. Furthermore, the gratitude of the authors is for Martin Achner and Daniel Habegger for their work and support in performing the wind tunnel tests in the TMK facility, without whom the testing would not have been possible otherwise.

References

[1] C. Hantz, A. Marwege, J. Klevanski, B. Reimann, G. De Zaiacomo, R. Marey, J. Gutiérrez, G. Medici, A. Kopp and A. Gülhan, "SUPERSONIC BRAKING DEVICES FOR REUSABLE UPPER STAGES – OVERVIEW OF ROCKETHANDBRAKE," in *2nd International Conference on Flight Vehicles, Aerothermodynamics and Re-entry Missions & Engineering (FAR)*, Heilbronn, 2022.

[2] G. De Zaiacomo, "Mission Engineering and Control Design for the Recovery of a Heavy Launcher Upper Stage," in *Ascention*, Dresden, 2023.

[3] S. Langer, A. Schwöppe and N. Kroll, "The DLR Flow Solver TAU - Status and Recent Algorithmic Developments," 52nd Aerospace Sciences Meeting, National Harbor, Maryland, USA, January 2014.

[4] P. Spalart and S. Allmaras, "A one-equation turbulence model for aerodynamic flows," in *AIAA Paper 1992-0439*, 1992.

[5] M. Laureti and K. Sebastian, "Aerothermal databases and load predictions for Retro Propulsion-Assisted Launch Vehicles (RETALT)," *CEAS Space Journal* , 2022.

[6] A. Schuster, L. Reimer and J. Neumann, "A Mesh-free Parallel Moving Least-Squares-based Interpolation Method for the Application in Aeroelastic Simulations with the FlowSimulator," *New Results in Numerical and Experimental Fluid Mechanics X*, 2016.

[7] M. Ertl and T. Ecker, "Aerothermal analysis of plume interaction with deployed landing legs of the CALLISTO vehicle," *EUROPEAN CONFERENCE FOR AERONAUTICS AND AEROSPACE SCIENCES (EUCASS)*, 2022.

[8] J. Kim, "Pre- and Postflight Thermal Analysis of Test Launch Vehicle Fuselage," *JOURNAL OF SPACECRAFT AND ROCKETS*, vol. 56, no. 6, 2019.